ADVANCED MATERIALS
www.advmat.de

Magnetic Topological Insulator Heterostructures: A Review

Jieyi Liu and Thorsten Hesjedal**

Topological insulators (TIs) provide intriguing prospects for the future of spintronics due to their large spin–orbit coupling and dissipationless, counter-propagating conduction channels in the surface state. The combination of topological properties and magnetic order can lead to new quantum states including the quantum anomalous Hall effect that was first experimentally realized in Cr-doped $(Bi,Sb)_2Te_3$ films. Since magnetic doping can introduce detrimental effects, requiring very low operational temperatures, alternative approaches are explored. Proximity coupling to magnetically ordered systems is an obvious option, with the prospect to raise the temperature for observing the various quantum effects. Here, an overview of proximity coupling and interfacial effects in TI heterostructures is presented, which provides a versatile materials platform for tuning the magnetic and topological properties of these exciting materials. An introduction is first given to the heterostructure growth by molecular beam epitaxy and suitable structural, electronic, and magnetic characterization techniques. Going beyond transition-metal-doped and undoped TI heterostructures, examples of heterostructures are discussed, including rare-earth-doped TIs, magnetic insulators, and antiferromagnets, which lead to exotic phenomena such as skyrmions and exchange bias. Finally, an outlook on novel heterostructures such as intrinsic magnetic TIs and systems including 2D materials is given.

1. Introduction

Quantum transport phenomena such as giant magnetoresistance,[1,2] high-temperature superconductivity,[3] and the quantum Hall effect (QHE)[4,5] have been extensively studied over the last decades. The QHE is particularly important as it has been the seed for topological research in condensed matter physics. A topologically non-trivial material is characterized by a topological number, such as the Chern number, which remains unchanged under continuous deformations.[6,7] The QHE was first discovered in 2D electron gas systems in large out-of-plane magnetic fields.[4] The QHE is the quantized version of the classical Hall effect whereby its Hall conductance is quantized Ce^2/h, where C is the Chern number (an integer), e is the elementary charge, and h is the Planck constant. The Chern number corresponds to the occupancy of discrete Landau levels, which can be varied by tuning the Fermi energy via a gate voltage. It further corresponds to the number of dissipationless conduction channels in the gapless edge state of the quantum Hall insulator that is insulating in the bulk in high magnetic fields.

After observing the quantum version of the Hall effect, the natural question to ask is if there is also a quantized version of the anomalous Hall effect (AHE), commonly observed in ferromagnets. This quantum anomalous Hall effect (QAHE) would then be observable in the absence of external fields. The QAHE was initially proposed to arise in 2D honeycomb or kagome lattices, such as monolayer graphene, that host a non-zero out-of-plane magnetic flux density, but zero net flux in each unit cell.[8,9] Later, it was also proposed that the QAHE may be found in $Hg_{1-y}Mn_yTe$ quantum wells without an external magnetic field, in which the effect arises purely due to the spin polarization of the Mn atoms.[10] However, the experimental realization of the QAHE was not reported until 2013, when transport in 3D topological insulators (TIs) doped with magnetic impurities was studied. TIs refer to a class of materials that is insulating in the bulk, but which possess topologically protected conducting surface states. Right from the start, the field was (see refs. [6,11–17]), and continues to be (see refs. [18–20]), to a large degree driven by theory. Common examples of 3D TIs are rhombohedral Bi_2Se_3, Bi_2Te_3, and Sb_2Te_3.[15] The surface state of a TI consists of two linearly dispersing states connecting the bulk conduction and valence bands. The two states cross at one point in reciprocal space, the Dirac point (**Figure 1**a). The charge carriers in this band structure are massless fermions, which are described by the relativistic Dirac equation.[15] Due to the strong spin–orbit coupling (SOC) in these materials, surface electron spins are locked to their momentum, forming dissipationless, counter-propagating conduction channels in the surface state.

By introducing magnetism to a TI, either by impurity doping with magnetic elements, by proximity coupling to a magnetic insulators (MIs), or other magnetic layers, time-reversal symmetry (TRS) can be broken. TRS breaking can induce a bandgap in the surface states, leading to the realization of the QAHE which is characterized by 1D chiral edge conduction in zero-field at remanence, as shown in Figure 1. The Chern number, here being +1 or –1, corresponds to the direction of the spin-momentum locked edge current that can be flipped by a (small) external field. Using first-principles calculations, Sb_2Te_3, Bi_2Te_3,

Dr. J. Liu, Prof. T. Hesjedal
Clarendon Laboratory
Department of Physics University of Oxford
Parks Road, Oxford OX1 3PU, UK
E-mail: Jieyi.Liu@physics.ox.ac.uk; Thorsten.Hesjedal@physics.ox.ac.uk
The ORCID identification number(s) for the author(s) of this article can be found under https://doi.org/10.1002/adma.202102427.

DOI: 10.1002/adma.202102427

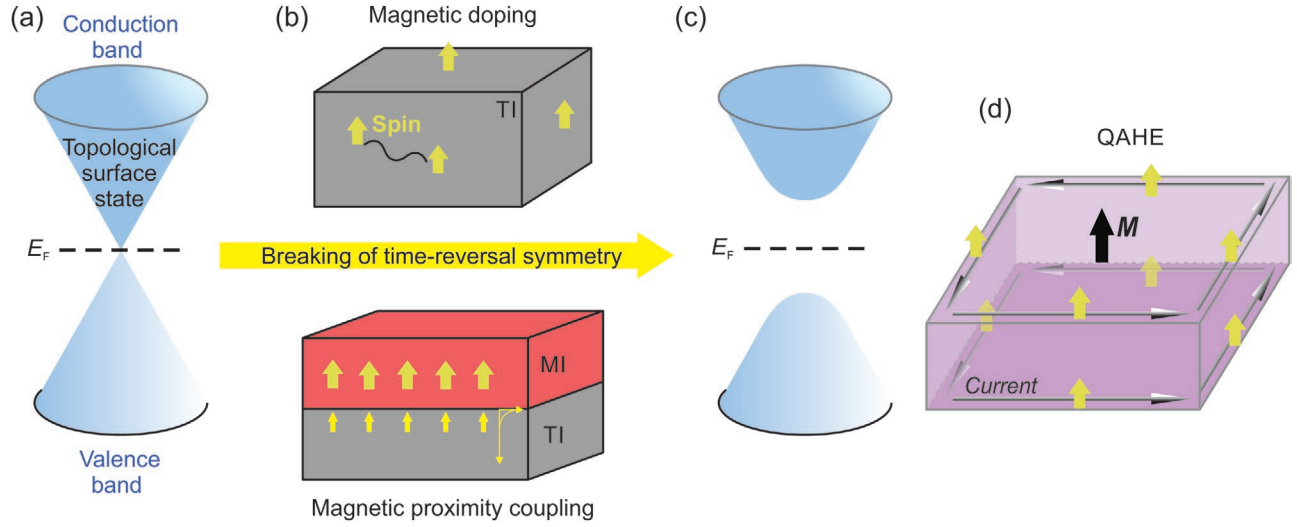

Figure 1. Schematic showing the change in the surface states of TIs by introducing magnetic order. a) Linearly dispersed topological surface state, with the Fermi energy (E_F) residing at the Dirac point. b) Breaking of time-reversal symmetry by bringing magnetic order to the TI system, either by doping with magnetic impurities or proximity coupling to a magnetic insulator (MI). c) Gapped surface state due to the magnetic order, with the Fermi energy residing in the bandgap. d) Realization of the QAHE in a TRS-broken TI material, showing quantized edge conduction at the top and bottom surfaces of the film, with the spin locked to the momentum.

and Bi_2Se_3 films were predicted to become possible QAH insulators by doping with magnetic impurities such as Fe or Cr.[21] Experimentally, the QAHE was first realized in 5 nm-thick, Cr-doped $(Bi,Sb)_2Te_3$ (Cr:BST) films on $SrTiO_3$ substrates.[22] The Hall resistivity of Cr:BST reached the quantized value of h/e^2 at 30 mK, which was significantly below the magnetic transition temperature of 15 K. This discrepancy between the two temperatures was later explained by the large Dirac-mass disorder, which has been independently confirmed through several experimental techniques, including spectroscopic imaging scanning tunneling microscopy,[23] scanning superconducting quantum interference device (SQUID) microscopy,[24] and electrical transport.[25,26] An uneven spatial distribution of magnetic dopants was discovered in the host material, resulting in an inhomogeneous bandgap size across the whole TI surface, depending on the local density of the dopants and the subsequent variations in magnetic order.

Taking inspiration from ordinary ferromagnetic heterostructures, proximity coupling has also been used for TI materials to achieve magnetic order, and thus enable the observation of topological phenomena at higher temperatures.[27,28] In contrast to ordinary ferromagnetic heterostructures, however, the proximity effect on TIs may be restricted to a shallower depth below the interface, and may or may not involve the topological surface state carriers to mediate the coupling between the local magnetic moments. In addition, the proximity approach brings about another advantage—a partial decoupling of the order-enhancing effect from the doping concentration in the TI. As with all doped materials, dopants introduce detrimental effects such as lattice defects, microscopic phase segregation, and impurity bands. Proximity coupling can break the TRS while maintaining the TI surface free from impurities, overcoming the problem of large Dirac-mass disorder.

Figure 2 shows the zero-field QAHE temperature (T_{QAHE}) chart for the different QAH insulators since 2013, most of which are described in detail in Section 2.3. It is apparent that a large majority of the successful materials are the result of further engineering of $(Bi,Sb)_2Te_3$ (BST) films using both magnetic doping and proximity coupling, with only three exceptions that were reported in early 2020. The year 2015 saw the observation of the QAHE in V-doped BST films at 120 mK and modulation-doped [Cr:BST/BST] pentalayer heterostructures at 2 K.[29,30] In 2018, the QAHE was observed in co-doped (Cr,V):BST films at 1.5 K[31] and in 2019 in proximity-coupled (Zn,Cr)Te/BST/(Zn,Cr)Te heterostructures at 1.5 K,[32] in which (Zn,Cr)Te is a ferromagnetic insulator. Finally, in 2020, both the QAHE and exchange bias effects were simultaneously observed in CST/Cr_2O_3 (T_{QAHE} = 100 mK), in which Cr_2O_3 is an antiferromagnetic insulator. Also, the topological Hall effect (THE) was found in CST/BST/CST heterostructures (T_{QAHE} = 0.4 K),[33] with further experiments confirming the presence of magnetic skyrmions. What is most remarkable in 2020 is a departure from the established BST family. Twisted bilayer graphene (TBG) aligned to hexagonal boron nitride has a T_{QAHE} of 3 K,[34] $MnBi_2Te_4$ single crystal flakes show a T_{QAHE} of 1.4 K,[35] and its close relative, $[MnBi_2Te_4/Bi_2Te_3]$ superlattices reach QAHE at a record-breaking 7 K.[36] Clearly, using heterostructures not only increases the temperature of quantized edge conduction, but also leads to the appearance of other exotic phenomena in TIs, perhaps leading to room-temperature spintronic devices.

With this review, we try to introduce the field of magnetic TI (MTI) heterostructures in the context of the techniques used to study their remarkable properties. The review is organized as follows: In Section 2, we describe the growth and doping of TI films, structural characterization techniques, and angle-resolved photoemission spectroscopy (ARPES) for band characterization. In Section 3, we present several magnetic characterization techniques with different lateral and depth resolving power. In Section 2.3, we provide a detailed review of MTI single-layer films and heterostructures of different kinds: QAH

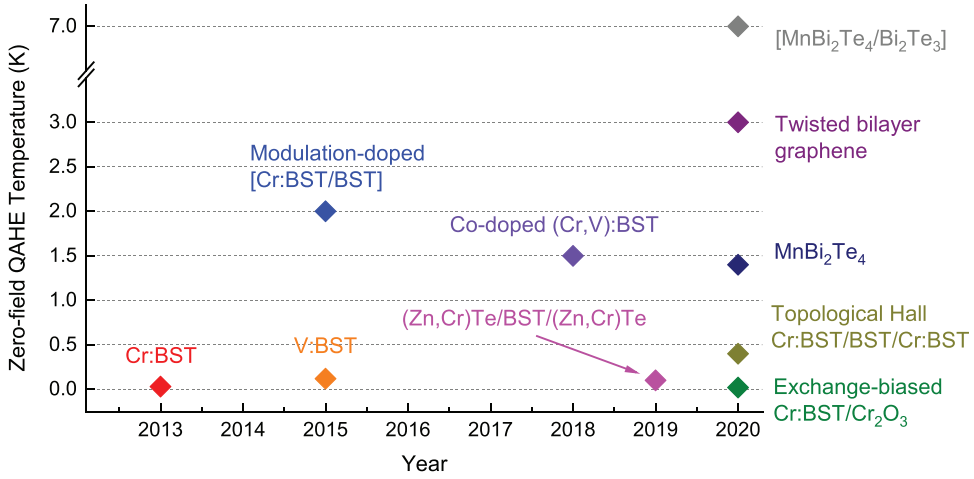

Figure 2. Timeline of the temperature performance of QAHE quantum materials (at zero external field). 2013: Cr-doped BST film at 30 mK;[22] 2015: V-doped BST film at 120 mK,[29] and modulation-doped [Cr:BST/BST] heterostructure at 2 K;[30] 2018: Co-doped (Cr,V):BST film at 1.5 K;[31] 2019: MI/TI/MI sandwich structure (Zn,Cr)Te/BST/(Zn,Cr)Te at 100 mK;[32] 2020: twisted bilayer graphene at 3 K,[34] intrinsic magnetic TI $MnBi_2Te_4$ flakes at 1.4 K,[35] [$MnBi_2Te_4/Bi_2Te_3$] superlattice at 7 K,[36] Cr:BST/BST/Cr:BST sandwich structure at 0.4 K (which also demonstrates the topological Hall effect[232]), and Cr:BST/Cr_2O_3 heterostructure at 20 mK (which also demonstrates exchange bias[33]).

insulators, MI/TI heterostructures, rare-earth (RE)-doped films, exchange-biased heterostructures, and heterostructures with skyrmions. Finally, in Section 5, we draw a conclusion and raise perspectives on the future development of MTI heterostructures and topological quantum materials in general.

2. Topological Insulator Thin Films: Growth, Doping, Structural, and Electronic Properties

For brevity, we will focus in this review on the established 3D TIs in the $(Bi,Sb)_2(Se,Te)_3$ family of solid solutions, most prominently Sb_2Te_3, Bi_2Te_3, and Bi_2Se_3. Much of the knowledge of this materials class is connected to their practical use as thermoelectric materials in cooling devices and generators since the late 1950s,[37] owing to their large room temperature figure-of-merit and the ability to easily achieve n- and p-type materials in the solid solution series.[38] Further, in the context of engineered TI heterostructures, we will restrict ourselves to the most versatile growth method, that is, molecular beam epitaxy (MBE). Apart from MBE, it is worth mentioning that magnetron sputtering, which is a more industry-friendly deposition method, has also been proven successful in the growth of TI films and heterostructures, including $Bi_xSe_{1-x}/Co_{20}Fe_{60}B_{20}$ and SmB_6.[39,40]

2.1. Thin-Film Growth

First reported for Bi_2Te_3 by Charles et al. in the context of thermoelectrics,[41] the MBE growth of TI thin films has been covered thoroughly in several excellent reviews.[42–44] We will therefore only briefly summarize the key elements of MBE growth, which has been achieved on a remarkable wide range of substrates owing to the relaxed requirement for lattice matching between film and substrate. Substrate for growing TI can be semiconductors such as Si,[45–48] Ge,[49,50] and GaAs,[51,52] while the most common substrate is Al_2O_3.[53–57] Amorphous substrates have also been used for TI growth such as SiO_2 and fused silica.[58–60] In all these cases, even with the lattice mismatch reaching 43.8% for Bi_2Te_3/ graphene,[43] the TI films usually grow *c*-axis oriented owing to their layered nature with weak interlayer chalcogen–chalcogen bonds. In fact, $(Bi,Sb)_2(Se,Te)_3$ compounds [space group D_{3d}^5 ($R\bar{3}m$)] are composed of Se/Te–Bi/Sb–Se/Te–Bi/Sb–Se/Te quintuple layers (QLs), separated by the so-called van der Waals gap (**Figure 3**d), which is key to the much relaxed lattice matching requirement. On lattice-matched substrates such as InP[61,62] (lattice mismatch 0.16% for Bi_2Se_3/ InP(111)B) and BaF_2[63,64] (lattice mismatch <0.04% for Bi_2Te_3/ BaF_2(111)), however, the films show no twinning, that is, they are also ordered in-plane. In general, van der Waals epitaxy, as introduced by Koma,[65] is characterized by the lack of lattice matching between film and substrate in the presence of the van der Waals interaction; however it does not necessarily mean that there cannot be in-plane alignment as well.

For the MBE growth of $(Bi,Sb)_2(Se,Te)_3$ thin films, Bi and/ or Sb and Se (or Te) are co-evaporated out of conventional effusion or special cracker cells. The growth window is typically very wide with substrate temperatures reported between 200 and 300 °C.[43,66] A two-step growth recipe is often used whereby the TI seed layer is grown at a lower temperature than the remainder of the layer.[56] For reducing chalcogen vacancy defects, the growth is usually conducted with a relatively high chalcogen overpressure of >5:1. The film structure, quality, and morphology are commonly monitored in situ using reflection high-energy electron diffraction (RHEED) to give a direct feedback on the growth, and ex situ using atomic force microscopy, X-ray diffraction, and reflectometry, as well as transmission electron microscopy. These techniques will be introduced in Section 2.4.

2.2. Doping

Doping of TI thin films is usually carried out with the goal of reducing the detrimental contribution of bulk carriers, to align

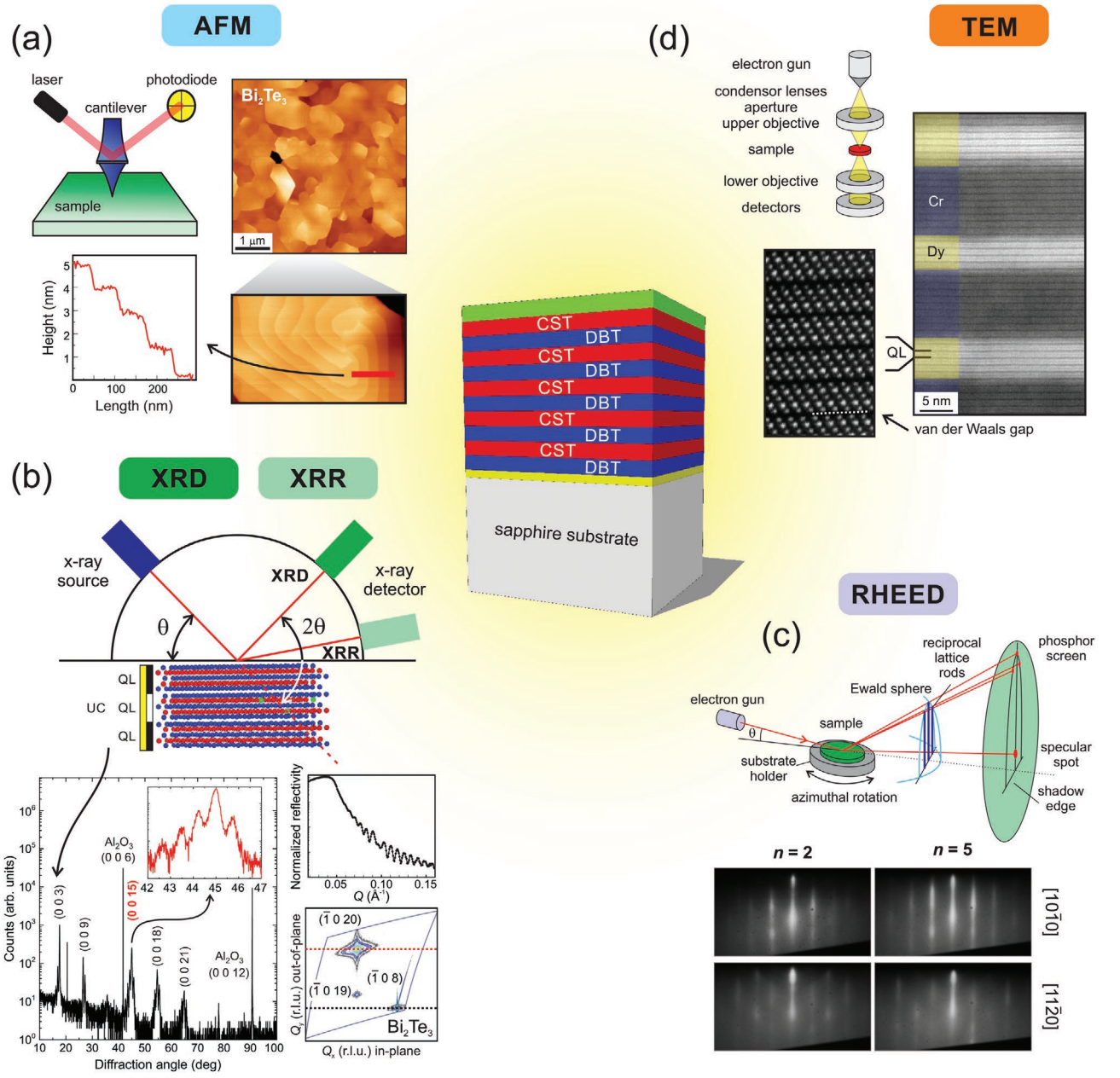

Figure 3. Structural characterization of TI thin films and heterostructures. Most examples here are results obtained from [Cr:Sb_2Te_3(CST)/Dy:Bi_2Te_3(DBT)] superlattices (depicted in the center). a) AFM is commonly used to study the surface topology of a sample ex situ. The investigated TI materials are characterized by terraced islands. The step height is usually 1 QL (≈1 nm). b) XRD and XRR are used to determine the crystal structure of the films, including the effects of doping and growth conditions and the layer thicknesses and interfacial roughnesses, respectively. Reciprocal space mapping is generally used to take a closer look at multiple substrate and film reflections, revealing strain effects. X-ray diffraction techniques are usually applied ex situ; however, in situ grazing-incidence XRD is possible at synchrotron beamlines. c) In situ RHEED image of the TI heterostructure after 2 and 5 bilayer repeats along the [10$\bar{1}$0] azimuth (upper row) and [11$\bar{2}$0] azimuth (lower row) of sapphire substrate. d) Ex situ TEM is the most common microscopy technique for studying TI films. It reveals the layer stacking (here through elemental contrast of the Dy and Cr dopants) and the detailed QL structure with the separating van der Waals gap. In combination with energy-dispersive X-ray spectroscopy, electron microscopy reveals the elemental composition as well. XRD/XRR plots in (b) and RHEED images in (c): Reproduced with permission.[87] Copyright 2018, American Physical Society. Reciprocal space map: Reproduced under the terms of the CC-BY Creative Commons Attribution 4.0 International license (https://creativecommons.org.licenses/by/4.0).[83] Copyright 2015, The Authors, published by Springer Nature. d) TEM image: Reproduced with permission.[88] Copyright 2019, American Physical Society.

the Fermi level in the middle of the bandgap, or to introduce magnetic ordering in the TI, whereas it is straightforward to make the semiconductor Bi_2Te_3 p- or n-type by alloying with Sb_2Te_3 or Bi_2Se_3 in the same solid solution, respectively,[38] explaining its success as a thermoelectric material, controlled impurity doping is more of an issue.[67] Another challenge is

making electrical contacts to these thermoelectric materials since interfacial reactions are very common,[68–70] with the possibility of a complete dissolution of the thin film.[70] The formation of secondary metal chalcogenides can prevent further deterioration of the film;[69] however, this is not a solution for the electronic or magnetic doping of TIs, where such reactions have to be prevented and be controlled, and where the goal is to achieve substitutional doping of the films.

In an attempt to achieve bulk-insulating TIs with high mobilities, it is most straightforward to stay in the $(Bi,Sb)_2(Se,Te)_3$ solid solution series. Indeed, in quaternary $Bi_{2-x}Sb_xTe_{3-y}Se_y$, the topological surface states (TSSs) are well developed and the QHE was observed.[71] However, for achieving the QAHE and for unlocking other quantum effects, TRS has to be broken either by direct magnetic doping or proximity coupling (see Section 2.3). In MBE growth, the dopants are co-evaporated together with the other constituent elements, and their desired concentrations are adjusted via their ratio to the combined group V element flux. In the extreme case, doping can be controlled on the level of atomically thin layers. The homogeneous magnetic doping of TI thin films has been achieved with both transition metal and rare earth elements.

In the case of transition metals, ferromagnetic order has been demonstrated for $Cr:Bi_2Se_3$,[72] $Cr:Sb_2Te_3$,[73] $Cr:(Bi,Sb)_2Te_3$,[29] $V:Bi_2Se_3$,[74] $V:(Bi,Sb)_2Te_3$,[29] $V:Sb_2Te_3$,[75] and $Mn:Bi_2Te_3$.[76] In all cases, the dopants are incorporated substitutionally on the Bi/Sb sites up to a critical concentration which varies greatly between 0.6 % and 21%. The most important systems are Cr- and V-doped Sb_2Te_3, showing out-of-plane anisotropy with ferromagnetic transition temperatures of 59 and 104 K, respectively.[29] Long-range magnetic order in these systems is studied usually by magnetometry, X-ray magnetic circular dichroism, and polarized neutron reflectometry,[72,77–79] which will be discussed in detail in Section 3.

Rare earth doping was inspired by the prospect to introduce a very high magnetic moment ion into the TI, thereby increasing the size of the magnetic gap, and further encouraged by the similar ionic radii for substitutional doping. However, despite having achieved substitutional doping of high-quality Bi_2Te_3 films with Gd, Dy, and Ho,[80–82] all films remained essentially paramagnetic with some hints of antiferromagnetic behavior.[80–84] Although Eu-doped Bi_2Se_3 has demonstrated ferromagnetism with over 10% Eu concentration, the doing profile in this system is not uniform,[85] which is an issue for transport measurements. Nevertheless, for Dy doping, it is already shown that low fields of 0.65 T can result in induced moments on the order of ≈1/3 of the full Dy^{3+} moment in $Dy:Bi_2Te_3$.[86] Dy dopant therefore lends itself to being incorporated in heterostructures, in which the proximity to transition-metal-doped ferromagnetic layers "kick" the Dy-doped layer to be ordered as well.[87,88]

2.3. Heterostructure Growth

Making TI heterostructures with precisely controllable physical properties is a promising way to both add functionality and to overcome the challenges of magnetic doping, that is, by not adding dopants in the electronically active layers in the first place. The key of heterostructure engineering is proximity coupling between layers, which can be grown as part of the TI stack or separately, that is, in a different deposition chamber or transferred into the MBE system through the load-lock. In case of non-magnetic TIs, proximity coupling can align the spins of the TSS carriers, leading to exchange splitting.

There are a number of strategies for making use of magnetic proximity effects in TI heterostructures, which will be described in detail in Section 2.3:

(i) modulation doping,[30]
(ii) coupling to magnetic insulators such as $Y_3Fe_5O_{12}$ or $Tm_3Fe_5O_{12}$ with the desirable perpendicular magnetic anisotropy,[89,90]
(iii) direct evaporation of ferromagnetic layers,[84,91–93]
(iv) superlattices of large moment and high transition temperature layers,[87] and
(v) coupling to antiferromagnets.[94] $CrSb/Cr:(Bi,Sb)_2Te_3$ is an example for the latter,[94] in which the chemical and structural compatibility between the two materials leads to high quality, abrupt interfaces.

This idea has been further developed and brought to perfection in the form of $MnBi_2Te_4/Bi_2Te_3$, which is part of the $(MnBi_2Te_4)_m(Bi_2Te_3)_n$ homologous series.[95,96] As such, interfaces between dissimilar materials are absent since $MnBi_2Te_4$ is effectively terminated by a layer of Bi_2Te_3, making this so-called intrinsic MTI the ideal material platform for the exploration of topological quantum effects. In fact, ordered $MnBi_2Te_4/Bi_2Te_3$ heterostructures can be achieved by doping Bi_2Te_3 with Mn. However, instead of forming disordered $Mn:Bi_2Te_3$ layers, a self-organized heterostructure with alternating $MnBi_2Te_4$ septuple layers (SLs) and Bi_2Te_3 QLs has been obtained in thin films.[97] A similar observation has been made in case of $MnBi_2Se_4/Bi_2Se_3$ heterostructures which form through self-organization in Mn-doped Bi_2Se_3 during MBE growth.[98] Note that due to the self-organized nature of the heterostructure formation, these ordered heterostructures have in fact been first realized in bulk crystals,[95,99] leading to the prediction[18,100] and first observation of antiferromagnetic TIs.[18,99] However, as the properties of these heterostructures alternate between intrinsic QAH insulator and axion insulator depending on even/odd layer repeats, thin-film growth is more suitable for fabricating device structures.

2.4. Structural Characterization

In this section, the common structural characterization techniques are illustrated, using the results obtained from a $[Cr:Sb_2Te_3(CST)/Dy:Bi_2Te_3(DBT)]$ superlattice as an example (schematic depicted in the center of Figure 3). The structural characterization of TI films and heterostructures relies on the standard techniques used for any MBE-grown materials, that is, ex situ atomic force microscopy (AFM), X-ray diffraction (XRD) and reflectivity (XRR), transmission electron microscopy (TEM) with energy-dispersive X-ray spectroscopy (EDS) for elemental analysis, and in situ RHEED. More rarely, for the precise determination of the doping concentration, and sample

stoichiometry in general, Rutherford backscattering spectroscopy and particle-induced X-ray emission are employed.[80] In addition, synchrotron-based extended X-ray absorption fine structure can be used to gain insight into the doping scenario, for example, substitutional versus interstitial doping or incorporation in the van der Waals gap, along with the oxidation state of the dopants.[101,102]

In contrast to many other thin-film materials, the relative importance of AFM is undeniable for the study of TI films. This very accessible scanning probe technique maps the film morphology, providing insight into the growth mode and mechanism (top right panel in Figure 3a), as well as doping effects through structural changes. The key is that the films grow in a QL-by-QL fashion, with a QL step height of ≈1 nm being easily resolvable (bottom left panel in Figure 3a). The surface of the Bi_2Te_3 film on *c*-plane sapphire is characterized by terraced islands with the characteristic 1-QL steps. These islands show a type of spiral surface growth[103] (Figure 3a in the bottom right panel), which is explained by the pinning of QL growth fronts at irregular substrate steps.[104]

XRR and XRD measurements are usually carried out in lab-based diffractometers using Cu $K\alpha 1$ radiation. Typical reflection and diffraction geometries are illustrated in the top panel of Figure 3b. Apart from the layer thicknesses, the reflectivity oscillations in XRR (see top right panel in Figure 3b) also reveal interfacial roughnesses in heterostructures through comparison with models of the thin-film structure. Using XRD, the crystal structure of the films is confirmed via the analysis of the film peaks (bottom left panel in Figure 3b) and their structural quality is determined via the peak width. Superlattices further lead to a series of peaks, reflecting the numbers of repeated layers (see inset in the XRD scan on the left of Figure 3b). This is particularly useful for doping studies, whereby upon introducing dopants into the host, the film peaks broaden and shift position, allowing for a quantification of undesired degradation of the crystalline quality.[72,79] Apart from the very common out-of-plane θ–2θ XRD scans shown here, in-plane φ scans give access to the in-plane epitaxial relationships and allow for the detection of twinning, which is common for TI growth on most substrates.[64] Lattice strain can be revealed through the comparison with substrate peaks and by performing reciprocal space maps.[83] Although X-ray diffraction is usually an ex situ technique, in situ grazing-incidence XRD is also possible using synchrotron facilities, giving insight into the structural properties and their evolution during growth.[105]

The most common in situ characterization technique is RHEED, which provides online feedback about the film growth. In particular, it helps to optimize substrate preparation and growth recipes, by observing the diffraction patterns that are characteristic for the respective material. Figure 3c shows RHEED images taken along the $[11\bar{2}0]$ and $[10\bar{1}0]$ azimuths of *c*-plane sapphire during the growth of a [CST/DBT] superlattice after finishing two and five repeats. The streaky pattern is indicative of flat, crystalline surfaces, and a transition to a more diffuse pattern can be observed upon doping above a critical limit, which indicates a loss of crystalline order.[80–82] The azimuthal characteristic of the pattern (with respect to the substrate pattern) allows for the determination of the in-plane epitaxial relationships, and its symmetry shows possible twinning. It is important to note that RHEED in case of $(Bi,Sb)_2(Se,Te)_3$ TI films is a destructive technique, as the beam leaves a visible damage on the wafer, meaning that RHEED cannot be used continuously during growth.

Electron microscopy is particularly useful for the investigation of TI single layers and heterostructures in terms of film quality and defects, but also for acquiring direct microscopic evidence of doping-related material issues, such as diffusion and interfacial reactions that lead to secondary phases. For high-angle annular dark-field scanning transmission electron microscopy (HAADF-STEM) imaging, thin membranes of the sample are prepared by focused ion beam milling, or traditional preparation techniques if possible. A key challenge here is the softness and small resistance to shear, that makes it difficult to mechanically prepare the TI specimen on hard substrates such as sapphire. In Figure 3d, a cross-sectional overview of a [CST/DBT] superlattice is depicted on the right, clearly showing the Dy-doped (brighter, larger atomic number) and Cr-doped (darker, smaller atomic number) layers. Van der Waals gaps are located between the layers where no contrast can be seen, which are even more clearly visible in the close-up on the left where the QLs are fully resolved. For doping studies, EDS reveals the elemental composition and the precise location of the dopants in the TI host lattice.[83]

2.5. Angle-Resolved Photoemission Spectroscopy

ARPES provides the direct visualization of the electronic band structure of a solid.[106,107] Based on the photoelectric effect, photons incident on a material with sufficient energy to overcome the work function (typically a few eV) will result in the emission of electrons from the host material into the vacuum. These photoexcited electrons are then detected and their kinetic energy and emission angle are analyzed (see **Figure 4**a,b for details). Due to the conservation of momentum along the in-plane direction and the conservation of energy, the photoelectron analysis can be used to map out the 3D band dispersion of the material in momentum space.

The incident light used in the study of TIs is often in vacuum ultraviolet (VUV) range. The inelastic mean free path of electrons from VUV photoemission is on the order of 1 nm, meaning that it is mainly sensitive to the topmost layers of the sample. The surface sensitivity makes ARPES suitable for probing topological surface states of TI films. Some ARPES systems are based in university laboratories where a laser or discharge lamp is used as the light source, giving the advantage of easy integration with other ultrahigh vacuum (UHV) systems such as material deposition chambers and scanning tunneling microscopes, allowing for the investigation of pristine TI films. For example, the Dirac cone in the band structure of Bi_2Se_3 films was successfully observed using laser-ARPES.[108] However, laser/lamp-based ARPES is limited by the range of photon energies and small cross-sections for some materials of interest. Meanwhile, many synchrotrons operate ARPES beamlines, as synchrotron radiation provides a wide range of continuously tunable incident photon energy and high photon flux. This gives a more complete map of the bands in 3D momentum space, and photon-energy-dependent results can

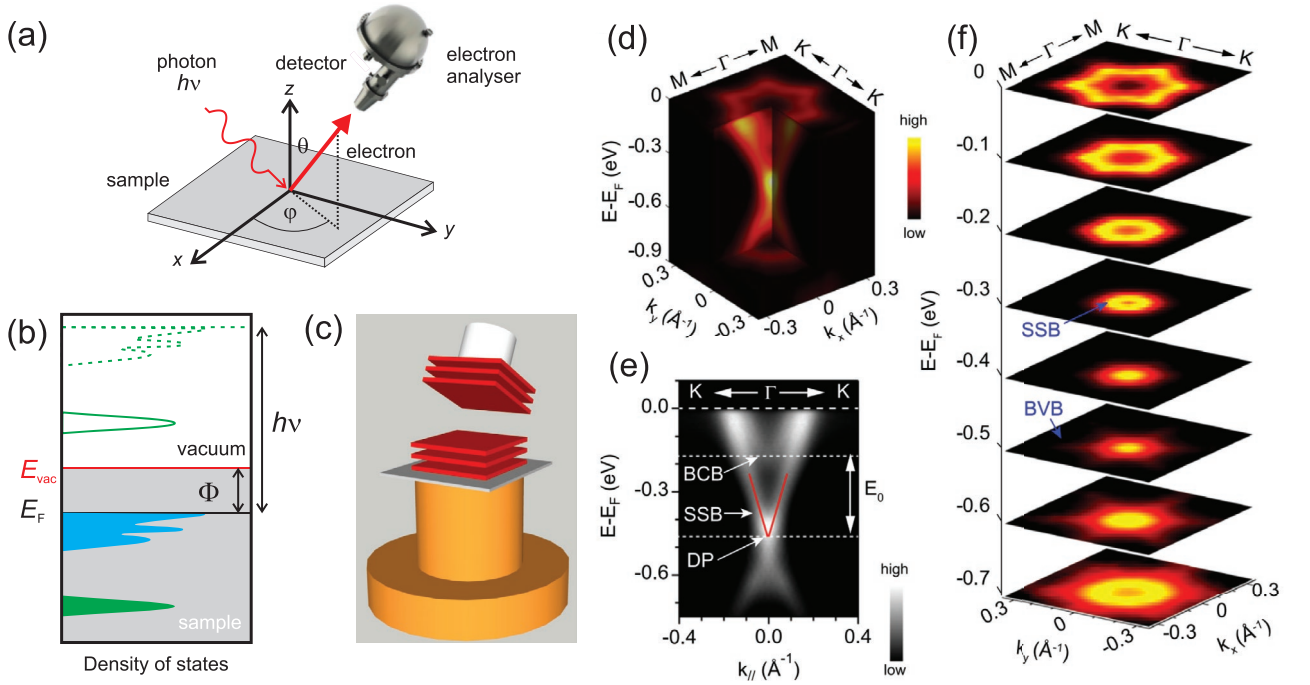

Figure 4. Study of TI systems using angle-resolved photoemission spectroscopy (ARPES). a) Schematic showing the working principle of ARPES. Incident photons of energy $h\nu$ can be absorbed by the sample, followed by the ejection of photoexcited electrons at an angle (θ, ϕ) from the surface of the material. These electrons then go through a hemispherical electron analyzer, finally reaching a detector. b) Energy diagram of the photoemission process. The difference between the vacuum energy (E_{vac}) and the Fermi level (E_F) equals the work function (Φ) of the material. c) Schematic showing the in situ cleaving process of a van der Waals thin film (in red) for ARPES. d) 3D band structure of a cleaved $(Gd_{0.1}Bi_{0.9})_2Te_3$ film after K dosing. e) Band structure of $(Gd_{0.1}Bi_{0.9})_2Te_3$ along the Γ–K direction, revealing the surface state band (SSB), bulk conduction band (BCB), and Dirac point (DP) with linear dispersion. f) Stack of constant energy maps of $(Gd_{0.1}Bi_{0.9})_2Te_3$ at different binding energies. c) Sketch: Reproduced with permission.[115] Copyright 2014, American Physical Society. d–f) Figures: Reproduced with permission.[116] Copyright 2014, American Physical Society.

be used to distinguish between the surface and bulk contributions. As a result, many groundbreaking results reporting TI band structures have been obtained using synchrotron-based ARPES.[109–112]

Since ARPES experiments require the film surface to be mirror-flat and free from contamination, and most TI films have to be transferred through air before reaching a synchrotron end station, it is important to develop sample preparation procedures for the recovery of pristine surface in the UHV chamber. Ar-ion sputtering and annealing can be partly effective in cleaning the TI surface; however, this process can also introduce defects and additional surface roughness.[113,114] Moreover, when transported through air, especially rare earth element doped TI samples are prone to oxidation. Another approach is to grow an amorphous Te or Se capping layer in situ in the MBE chamber, followed by decapping in the ARPES chamber via heating. This process, however, can lead to non-stoichiometric and rough films. Alternatively, in situ cleaving has been established for TI films,[115] similar to the standard ARPES preparation technique used for single crystals. First, a capped film is glued to the ARPES sample holder, followed by a small ceramic post glued to the cap. Then, in UHV, the post is struck by a wobble stick such that the TI film cleaves at a van der Waals gap, leaving a fresh TI surface exposed, as illustrated in Figure 4c. Using this technique, high-quality band structure data were obtained from rare-earth-doped Bi_2Te_3 films,[80,81,116] with representative results presented in Figure 4e,f.

3. Magnetic Properties of TI Thin Films and Heterostructures

The first step in the magnetic characterization of TI thin-film samples is usually to perform lab-based bulk magnetometry using SQUID. With SQUID, both the in-plane and out-of-plane magnetization can be probed; however, this requires the remounting of the sample and thereby changing the measurement configuration. The sample environment usually allows for measurements from 1.8 to 300 K, in an applied field of typically up to 7 T, which conveniently covers the interesting parameter range for most MTI materials. As the magnetic information obtained by SQUID represents the average over all layers of a sample, important information may remain in the dark, for example, the contributions of the individual layers or the presence of canted moments near the interfaces. Also, due to the usually very small ferromagnetic signal from MTI layers, the comparably huge diamagnetic (or paramagnetic) background coming from the substrate has to be carefully subtracted.

In this section, we will give an overview of some of the most common advanced magnetic characterization techniques, starting in Section 3.1 with X-ray- and neutron-based spectroscopy and reflectometry techniques, mostly giving a layer-resolved average of the magnetic properties. Next, we will summarize local characterization techniques in Section 3.2, both in the sense of microscopy and the local probing of the magnetic environment with muons. Finally, in Section 3.3,

we highlight the techniques capable of directly probing the QAH state including THz spectroscopy and standard electrical transport. In **Figure 5**, we summarize and compare the different methods in terms of their probing depth or volume and lateral resolution.

3.1. Layer-Resolved Heterostructure Properties

The layer-resolved characterization of magnetic heterostructures requires large-scale X-ray and neutron facilities that provide the necessary high intensities of energy-tunable incident waves. Whereas X-rays become sensitive to magnetic properties when tuned to a suitable absorption edge, neutrons carry a magnetic moment and interact directly with the magnetically ordered layers. In this section, we briefly review X-ray magnetic circular and linear dichroism, as well as polarized neutron reflectometry, which are most relevant for TI heterostructures (illustrated in the lower half of the main panel in Figure 5).

3.1.1. X-ray Magnetic Circular and Linear Dichroism

X-ray absorption spectroscopy (XAS) gives insight into the chemical composition and oxidation state of the elements of a thin-film sample. In an XAS experiment, the absorption of the X-rays is detected as a function of the incident photon energy, yielding element-specific core-to-valence state transitions. The absorption can be detected either via the secondary-electron-induced drain current in total-electron-yield (TEY) mode, fluorescence from the core hole decay in fluorescence yield (FY) mode, or the X-ray excited optical luminescence in the visible or near-visible spectral range in luminescence yield (LY) mode. The different modes are illustrated in Figure 5d. All three modes probe different depths of the sample depending on the element probed. As a rule of thumb, TEY probes surface-sensitively down to ≈4 nm at the Co edge,[117] and ≈6 nm at the Dy edge,[118] whereas LY will probe the entire film (for thicknesses below 200 nm). The depth sensitivity in FY mode is between TEY and LY, and often limited by saturation and self-absorption effects in highly doped TIs.[119]

In the absorption process on 3d transition metals, a core electron is excited from the spin-split 2p core states to the 3d valence state. When the incident X-rays are circularly polarized, left- and right-circularly polarized light has different transition probabilities into the unoccupied states for magnetic materials. Therefore, the transition probability depends on both the helicity of the incident light and the magnetic state of the sample. The X-ray magnetic circular dichroism (XMCD) signal is the difference between two XAS spectra obtained with different X-ray helicities, or opposite magnetization (for which the applied magnetic field would be reversed). As a result, XMCD is sensitive to the difference in the density of empty states with different spin polarizations. Apart from the $L_{2,3}$ edges in 3d transition metals, soft X-ray (energy typically <2 keV) XMCD can also be performed on the lanthanide $M_{4,5}$ edges. A typical XMCD spectrum at the Cr $L_{2,3}$ edges is shown on the left of Figure 5d, obtained by subtracting the XAS spectra measured with opposite circular polarizations. The element specificity of XMCD is particularly useful for the unambiguous confirmation of the electronic and magnetic state of transition metal and rare earth magnetic dopants in TIs.[82,120] Using the celebrated sum rules[121] on the integrated intensities over the absorption edges of the XMCD, the spin and orbital moments of the ground state can be determined. For an in-depth coverage of the topic, we refer to the reviews in refs. [117,122,123].

In order to precisely determine the critical temperature of magnetic transitions, and to gain deeper insight into the microscopic magnetic coupling scenario, Arrott–Noakes analysis of the temperature-dependent XMCD data can be performed.[124] The critical exponents β and γ can be obtained by plotting the isothermal variations of the magnetization $M^{1/\beta}$ as a function of the ratio of applied field H over M in the form of $(H/M)^{1/\gamma}$. In the case of XMCD, M is given by the background-corrected XMCD asymmetry. For Dy-doped Bi_2Te_3, critical exponents were found that are consistent with a 3D Heisenberg model,[84] instead of $\beta = 0.5$ and $\gamma = 1$ for the long-range mean-field model, which was found for Cr-doped Bi_2Se_3 films.[92]

X-ray magnetic linear dichroism (XMLD)[125] relies on the difference between XAS spectra of horizontal and vertical linear polarized light and can be used to study antiferromagnetic (AF) spin systems. It is mentioned here for completeness only; however, it is relevant as AF-coupled layers are at the core of intrinsic TIs,[35] and as AF ordering was found in lanthanide-doped TIs.[126,127]

To summarize, XMCD and XMLD are extremely useful for the study of the magnetic properties of TI films. The element-selectivity of the probe leaves no doubt about the origin of the magnetic ordering, the spin and orbital moments can be determined, as well as the oxidation state, and temperature-dependent studies give an insight into the ordering mechanism. Further, as a result of the depth-sensitivity of the three different detection modes, near-surface properties can be distinguished from the behavior of the bulk of the film, opening up ways for raising transition temperatures through proximity coupling.[92]

3.1.2. Polarized Neutron Reflectometry

Polarized neutron reflectometry (PNR) is ideally suited for determining the magnetic structure of multilayered materials systems,[128] not only allowing for the determination of the magnetization of the constituent layers but also, for example, of extended magnetization patterns, proximity effects, interlayer coupling, and the structure and transitions of antiferromagnets.[129] Although being a spatially averaging technique, providing layer resolution only, off-specular reflectivity also gives insight into the in-plane correlation of the magnetization.[130] The basic principle is similar to XRR in the sense that the reflected intensity is measured as a function of incident angle, yielding chemical contrast along the surface normal, that is, the depth profile of a layered sample. Characteristic periodic thickness fringes in the reflectivity are the result of constructive interference of the reflections from the different layers, whereas the overall fall-off of the curve is the result of interfacial and/or surface roughness. Different from XRR, however, neutrons possess a magnetic moment and therefore interact with the

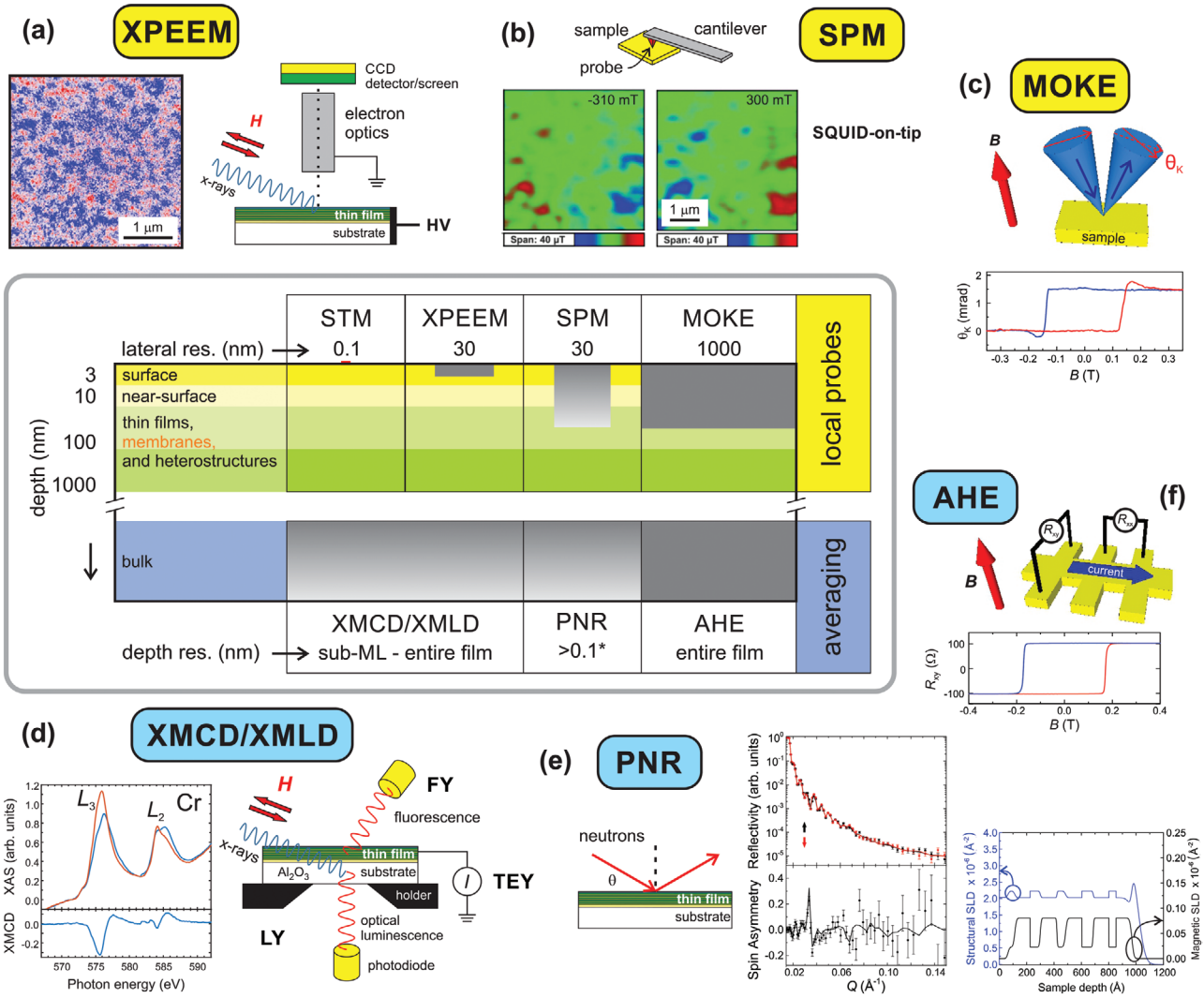

Figure 5. Comparison of different magnetic characterization techniques. Top row: spatially resolving techniques; bottom row: spatially averaging techniques. a) XPEEM provides the spatially resolved, element-specific magnetization near the sample surface with a resolution down to ≈40 nm. The image shows magnetic domains in Cr-doped Sb_2Te_3. b) Scanning probe techniques rely on a probe being mounted on a force-sensing device (here a cantilever). In this example, SQUID-on-tip microscopy images show the out-of-plane component of the magnetic stray field of a Cr:BST sample at 250 mK, in an opposite applied magnetic field of ≈300 mT, that is, the reversal of the magnetic domains is visible. c) MOKE is a surface-sensitive technique with a lateral resolution of ≈μm, which can be easily integrated within a cryostat.[145] d) XMCD and XMLD, which are carried out at synchrotrons, rely on the magnetic field or polarization-dependent XAS spectra and allow for the element-selective probing of the different forms of magnetic order. In TEY mode, the probing depth is ≈3–5 nm. In FY mode, the measurement is strongly material-dependent, and often limited by self-absorption and saturation effects. LY mode, on the other hand, probes the entire thin-film heterostructure. e) PNR is a neutron-based technique for the determination of the magnetic depth-profile down to the monolayer limit. The results shown are for the [CST/DBT] superlattice depicted in Figure 3. f) Electrical transport that probes the AHE is the key technique for studying MTIs, giving a magnetic response integrated over the commonly used, micrometer-sized Hall bars. AHE and MOKE measurements can be combined in a single system.[145] b) Adapted with permission.[24] Copyright 2015, The Authors, published by American Association for the Advancement of Science. Reprinted/adapted from ref. [24]. © The Authors, some rights reserved; exclusive licensee American Association for the Advancement of Science. Distributed under a CC BY-NC 4.0 license. d) Adapted under the terms of the CC-BY Creative Commons Attribution 4.0 International license (https://creativecommons.org/licenses/by/4.0).[267] Copyright 2019, The Authors, published by Springer Nature. e) Adapted with permission.[88] Copyright 2019, American Physical Society.

magnetic moments in the sample as well. In particular, when polarized neutrons scatter off a given layer magnetization, the scattering cross-section depends on their relative orientation. Therefore, in principle, the spin of the neutrons may flip in the scattering process, giving four different scattering channels, that is, flipping and non-flipping channels with spin and neutron moments aligned or anti-aligned. The reflectivity curves are commonly fitted using the GenX package,[131] yielding the magnetic and chemical depth profiles. Note that for the determination of the magnetic depth profile of magnetic TI layers, PNR without polarization analysis is sufficient, that is, the polarization of the reflected neutron is not analyzed.[88]

Figure 5e illustrates the PNR technique: when interacting with magnetic moments in the sample, reflectivity curves for

oppositely polarized incoming neutrons are different (top plot in the middle), giving a spin asymmetry (bottom plot in the middle). Both chemical and magnetic depth profiles (plot on the right) are obtained after fitting the data with an appropriate model. Note that PNR is only sensitive to the in-plane moments of the sample; out-of-plane moments cannot be probed. In principle, PNR can be sensitive to very thin magnetic layers, down to less than a nm, however, strongly depending on the overall properties of the specific sample giving enough contrast for that specific ultrathin layer. In the context of TIs, PNR has also been used to study proximity effects at the interface between magnetic insulators and TI layers,[132] antiferromagnets and TIs,[133] and the magnetic ordering in the intrinsic TIs as a function of septuple layer repeats.

3.2. Local Magnetic Properties

The probing of the magnetic contrast with lateral resolution is primarily a means to study magnetic domains.[134] This field goes back to the Bitter decoration technique in the 1930s,[135] but is still highly relevant nowadays for developing magnetic data storage and sensor technologies. As domains can be rather large, depending on the magnetic properties of the sample and its geometry, the micrometer resolution provided by magneto-optic Kerr effect (MOKE) microscopy is sufficient for the study of many relevant magnetic materials. Regarding MTIs, it is also important to spatially resolve domain walls as they can control the chiral edge conduction associated with the QAHE.[136] With scanning probe microscopy (SPM) techniques and XMCD-based photoelectron emission microscopy, it is possible to acquire a more detailed picture of magnetic domains and the structure of domain walls with a lateral resolution on the order of tens of nm. Even atomic resolution can be achieved using SPM, and, in combination with *I–V* spectroscopy, access to the electronic properties can be gained that is complementary to ARPES. Here, we refrain from covering *I–V* spectroscopy and electron microscopy techniques, such as Lorentz transmission electron microscopy,[137] scanning electron microscopy with polarization analysis,[138] and spin-polarized low-energy electron microscopy,[139] because these techniques have not yet been used extensively for MTI research. The capabilities of the local probes covered here are illustrated in the upper half of the main panel in Figure 5.

3.2.1. Magneto-Optical Kerr Effect Magnetometry

The magneto-optical Kerr effect describes the changes of light polarization upon reflection from a magnetic material.[140] This effect originates from the spin–orbit coupling of the magnetic medium, as the incoming light provides a perturbing electric field to the orbital momentum of the electrons in the material, which is coupled to the spin momentum.[141] The change in the polarization angle or ellipticity of the reflected beam is (to first order) proportional to the magnetization of the medium. Following the Rayleigh criterion, the incident light can be focused down to sub-micrometer in diameter using a laser of visible wavelength, making it a powerful tool to non-invasively investigate the local magnetic properties of thin films and microstructures. Analogous to the Kerr effect that tracks the change in the reflection, the Faraday effect describes the polarization change of the transmitted light, which is more convenient for investigating optically transparent materials.

With the measurement geometry depicted in Figure 5c, MOKE has been employed to supplement magneto-transport and SQUID magnetometry in confirming magnetism of MTI films.[142] Although the detection depth of MOKE is in this case not precisely known, the penetration of a visible laser into heavy metals is known to be around 30 nm,[143] which provides an estimate for the relevant lengthscale. A systematic study of CST films has been conducted, which showed good agreement between the MOKE and transport results for various doping levels.[144,145] Furthermore, by scanning the laser spot across the film, MOKE magnetometry was used to determine the position of the edge of the EuS layer in EuS/Bi_2Se_3 heterostructures.[146] Moreover, a high-power laser can locally heat up a small area of the film and reduce the coercivity of a small spot, thereby allowing writing and erasing of arbitrary patterns in MTI films.[147] Finally, depending on the angle of incidence, polar MOKE and longitudinal MOKE can detect spins in out-of-plane and in-plane directions, respectively, giving insight into the domain wall of flipping spins in $Bi_2Se_3/Y_3Fe_5O_{12}$.[148]

Apart from the laser scanning microscopes discussed above, wide-field MOKE microscopy provides a direct 2D visualization of magnetic features in a thin film, with a broadband source to evenly illuminate the whole sample of interest by polarized light.[149] Utilizing its real-time resolving power, wide-field MOKE microscopes have been used to image magnetic skyrmion bubbles in heavy-metal/ferromagnet bilayer films.[150] Another application example is the real-time imaging of magnetization switching in Bi_2Se_3/Py heterostructures, which is driven by spin–orbit torques.[151]

3.2.2. Scanning Probe Microscopy

SPM offers a versatile platform for the exploration of the magnetic properties of thin-film samples and devices, and moreover, of their electric and structural properties.[152] Here, we will focus on AFM-based techniques and leave scanning tunneling microscopy based techniques aside, as they have been mostly very successfully used for electronic spectroscopy of TIs.[153]

As illustrated in Figure 5b, a force sensor (here a cantilever) with an attached probe is raster-scanned over the sample at a certain distance above the surface, measuring the effective interaction force, and thereby collecting the desired magnetic information along with the topography signal. The most direct way of obtaining magnetic contrast is to use ferromagnetically coated cantilevers. In magnetic force microscopy (MFM), the magnetic contrast, stemming from the interaction of the out-of-plane component of the magnetic stray field with the tip, is convoluted with the topographical contrast. The lateral resolution is on the order of 30 nm.[154] MFM can be carried out in applied fields in atmosphere,[155] or in a superconducting magnet at low temperatures.[156] Note, however, that the maximum field applied to the sample is in practice limited by the coercive field of the tip.

As stated above, the AFM principle offers a versatile platform for the integration of other sensors, some of which are sensitive to magnetic sample properties, for example, scanning Hall probe microscopy,[157] SQUID microscopy,[158] and magnetic exchange force microscopy.[159] Especially SQUID microscopy (in form of the improved SQUID-on-tip design) has been used to investigate the magnetic domain pattern in Cr-doped $(Sb,Bi)_2Te_3$ films as shown in Figure 5b.[24] In their field- and temperature-dependent measurements, Lachman et al.[24] found that the magnetic order in these films is not long-range, but, instead, superparamagnetic or superferromagnetic domains emerge, while paramagnetic patches remain visible far below T_C.

Since magnetic order and electric transport are strongly intertwined in magnetic TIs, it is worth noting that there are also probes for the local conductivity of a thin-film sample. Microwave impedance microscopy has been developed to characterize the local complex conductivity of a material.[160] In the context of TIs, it has been used to directly visualize edge states in QAH systems, and to study their magnetic field evolution.[161] Finally, scanning gate microscopy is a simple way to perturb transport in a device under investigation by providing a local biasing field. It has been used in an impressive demonstration of its abilities to spatially resolve scattering sites in quantum spin Hall systems, that is, 2D TI systems, limiting non-dissipative transport in the helical edge channels.[162]

3.2.3. X-ray Photoemission Electron Microscopy

In combination with photoemission electron microscopy (PEEM), XMCD and XMLD (see Section 3.1.1) are at the core of the X-ray PEEM magnetic microscopy technique,[163] or XPEEM for short, with an element-selective lateral resolution of ≈30 nm (Figure 5a). In theory, the lateral resolution can be further improved down to a few nm using aberration-corrected electron optics.[164] XMCD-PEEM is well-suited for the study of ferromagnetic domains in, for example, $Cr:Sb_2Te_3$,[165] and XMLD-PEEM allows for the study of antiferromagnetic films. Note, however, that the films have to be conductive. The depth sensitivity of XPEEM is determined by the mean free path of the secondary electrons, which is on the order of a few nm. While the temperature in XPEEM can be varied (typically between ≈100 K and elevated temperatures) due to a UHV environment, its precise control and stabilization is in practice not possible in most synchrotron-based setups. Further, the measurements can effectively only be carried out in small fields (of up to some 10 mT).[166] Finally, XPEEM also allows for time-resolved pump–probe experiments with a temporal resolution of 30–50 ps.[167]

3.2.4. Muon Spin Rotation

Muon spin resonance (μ^+SR) is the odd one out in this section, as "local" does not refer to the ability to produce laterally resolved images, but to probe the magnetic properties in the local environment of an implanted muon.[168] In a nutshell, in a μ^+SR experiment, a beam of highly spin polarized muons is implanted into the sample. Using accelerated high-energy protons to react with a graphite target, muons are obtained via the production of pions. At its stopping position, a muon experiences an effective magnetic field, which is the sum of local internal and applied external fields, leading to a characteristic precession of its spin at the Lamor frequency. Once the muon decays after a mean lifetime of 2.2 µs, a positron is emitted preferably along the direction of the muon spin at the time of the decay. By mapping the angular distribution of the positrons as a function of time, the time evolution of the statistical average direction of the spin polarization of the muon ensemble is obtained as the asymmetry function $A(t)$. Its decay is generally fast if static magnetic fields are present, whereas it is slow in a paramagnetic environment. As the decay of $A(t)$ is also sensitive to the spatial distribution and dynamical fluctuations of the local magnetic environment, valuable information about, for example, the spatial homogeneity of the magnetic order can be obtained. In combination with the ability to implant muons in a shallow region below the surface, so-called low-energy μ^+SR has proven invaluable for developing a microscopic picture of magnetic ordering in dilute magnetic semiconductor thin films,[169] which are in many ways comparable to magnetically doped TI films in that they show a coexistence of ferromagnetic and paramagnetic regions.[170]

3.3. Conductivity Probes for the Quantum Anomalous Hall State

3.3.1. Magneto-Transport

Magneto-transport measurements provide direct access to quantum conductance phenomena such as the QAHE and axion insulator state. Depending on the lowest temperature required, the measurement can be carried out in a ^{4}He cryostat (base temperature of ≈1.6 K), a ^{3}He cryostat (base temperature of ≈300 mK), or a dilution refrigerator (base temperature of ≈10 mK). The standard four-terminal measurement scheme is advantageous over the two-terminal counterparts, as it reduces the contribution of the resistance from the contact pads and wires. In order to measure the longitudinal and transverse resistances of the TI film, the sample needs to be fabricated into micrometer-sized Hall bar devices. The common Hall bar structure and experimental geometry are illustrated in Figure 5f, with an example hysteresis loop showing the AHE. For measurements on TIs, a gate voltage is applied to tune the location of the Fermi level with respect to the band edges. The gate potential can be applied from the top of the device through a nm-thin layer of dielectric material such as Al_2O_3, or, from the bottom of the device via a thin insulating or semi-insulating substrate.

Regarding the fabrication of Hall bar devices, in most cases, standard photolithography is used for TIs, followed by wet etching using acid solutions,[32] or dry etching using Ar ion beam bombardment.[171] Next, a Ti/Au layer is evaporated onto the sample to provide electrical contacts to the TI. The sample is then placed in a chip carrier and electrically connected up using Au wire bonding. Photolithography and wet/dry etching have been widely applied to fabricate TI heterostructures including QAH insulator structures.[30]

Apart from photolithography and wet/dry etching, mechanical scratching was initially used to produce Hall bar devices

from TI films.[31,172] In fact, the first QAH insulator device reported in the literature was fabricated via mechanical scratching.[22] In this approach, the TI film is first scratched by metal tips or scalpels to form a Hall bar, and then glued to a chip carrier using conductive silver paste. Ohmic contacts are formed by manually pressing In electrodes onto the Hall bar and then connecting them via Au wires to the chip carrier. This crude approach may have the advantage that the contamination is reduced since the sample is not exposed to acids or ion beams, however, the scratched devices are usually very large (a few millimeters). Also, they can only be fabricated one-by-one with very little control over the quality, making repetitive measurements impossible.

3.3.2. Terahertz Time-Domain Spectroscopy

As the photon energy of visible light is on the order of 1 eV, that is, significantly larger than the surface bandgap of MTIs (tens of meV), MOKE and Faraday effect measurements on TI films can excite charge carriers. On the other hand, the photon energy of terahertz (THz) radiation is only a few meV, which means that it is transmitted through MTI films without exciting carriers. Therefore, terahertz time-domain spectroscopy (THz-TDS) works as a powerful optical probe to investigate magneto-optical properties of topological surface states. In a THz-TDS experiment, ultrafast laser pulses excite a photoconductive emitter and receiver in the THz range, and the complex conductance of the material is obtained from analyzing the THz transmission through the TI film and substrate.

The complex Faraday and Kerr rotation of the TI material can also be detected using THz-TDS, by adding two wire-grid polarizers and a fast-rotating polarizer in the transmission geometry for polarization modulation.[173,174] In this case, the substrate works as an optical resonator to separate the transmitted light pulses in the time domain, with each pulse going through subsequently more reflections between TI surfaces before the final transmission. The first transmitted pulse provides information on the Faraday rotation and its subtraction from the second pulse provides the Kerr rotation. Using polarized THz-DES, the realization of the QAHE has been successfully confirmed in MTI heterostructures,[175] which revealed itself through quantization of the Faraday/Kerr angle that is related to the fine structure constant.[173,176]

4. Magnetic Heterostructures

4.1. Magnetic-Doped Quantum Anomalous Hall Insulators

Following the theoretical prediction that the magnetic dopants Fe and Cr can introduce the QAH insulator state in Sb_2Te_3, Bi_2Te_3 and Bi_2Se_3,[21] the structural, magnetic, and electronic properties of MBE-grown CST films were systematically investigated.[77,93,144] The crystal structure schematic is presented in **Figure 6**a, illustrating a rhombohedral lattice with Cr replacing Sb. Using XMCD, we have found that Cr 3d and Sb 5p moments are aligned parallel to each other, while the Te 5p moment is antiparallel to the former two.[93] Figure 6b shows the XRD spectra of $Cr_xSb_{2-x}Te_3$ for various doping levels. We have found that all $Cr_xSb_{2-x}Te_3$ films can remain of good crystallinity even for the highest doping level of $x = 0.76$. The magneto-transport results for $Cr_{0.58}Sb_{1.42}Te_3$ and $Cr_{0.76}Sb_{1.24}Te_3$ films are illustrated in Figure 6c. The longitudinal resistances of both films below the Curie temperature demonstrate a butterfly shape due to spin-dependent carrier scattering, which reaches a maximum around the magnetization reversal. The hysteresis loops revealed in the Hall resistance graph confirm the out-of-plane long range ferromagnetic order. Using Kouvel–Fisher plots, we obtain Curie temperatures of 132 K for $x = 0.58$, and 176 K for $x = 0.76$, respectively.[144] The record transition temperature reported for $Cr_xSb_{2-x}Te_3$ is 190 K for $x = 0.59$.[73] Note that the differences in transition temperatures for a nominal doping concentration are due to both, the different definition and method used for obtaining the transition temperature, and the technique used for determining the doping concentration. In general, the transition temperatures for MBE-grown thin films are much higher than for doped bulk crystals owing to the lower solubility limit in the bulk (e.g., $x = 0.095$ in bulk $Cr_xSb_{2-x}Te_3$ leading to a transition temperature of 20 K[177]).

While our studies on Cr:Sb_2Te_3 were underway, the QAHE was first experimentally realized in 5 nm-thick Cr:BST films.[22] By tuning the voltage of the back gate (V_G) to –1.5 V, the Fermi level resided in the surface bandgap, and the Hall resistivity reached the quantized value of h/e^2 at 30 mK, a temperature accessible by dilution refrigerators but not by He cryostats. As mentioned earlier, this temperature is significantly below the Curie temperature at 15 K due to the large Dirac-mass disorder.[23] After the initial success of observing quantized edge conductance in Cr-doped BST at 30 mK and then in V-doped BST at 120 mK,[29] many experimental attempts have been made to increase the realization temperature of the QAHE, mostly by changing the doping scheme in BST.[30,31,171,178] Among these attempts, two specific approaches of material doping can be highlighted in particular. The first approach is the co-doping. By co-doping BST with both Cr and V simultaneously, the Hall conductance of the material can stay close to the quantum regime up to 1.5 K.[31] It was suggested that the co-doping provides the combined effect of a large magnetic moment (from Cr) and a strong perpendicular anisotropy (from V), overall resulting in a large out-of-plane moment in the host material. As a result the surface bandgap can be sustained to a higher temperature in the co-doped BST film. It should be noted though that we also experimented the co-doping scheme of Cr and V but on Sb_2Te_3 films. We found that V works as a surfactant which undesirably prevents the substitutional doping of Cr into Sb sites, leading to the formation of the secondary phase Cr_2Te_3.[145,179]

Apart from co-doping, the other highlighted approach to QAH insulators is modulation doping in heterostructures,[30] that is, periodically inserting a doped Cr:BST layer during the growth of non-doped BST films, a technique that had been applied to $GaAs/Al_xGa_{1-x}$. As semiconductor heterostructures to achieve a high carrier mobility.[180] In the study of modulation doping, several types of [Cr:BST/BST] films were engineered: Cr:BST single-layer, Cr:BST/BST/Cr:BST bilayer, and BST/Cr:BST/BST/ Cr:BST/BST pentalayer. The layer schematics and corresponding transport results are demonstrated in Figure 6d. It can be seen that, the Hall resistance of the single-layer film

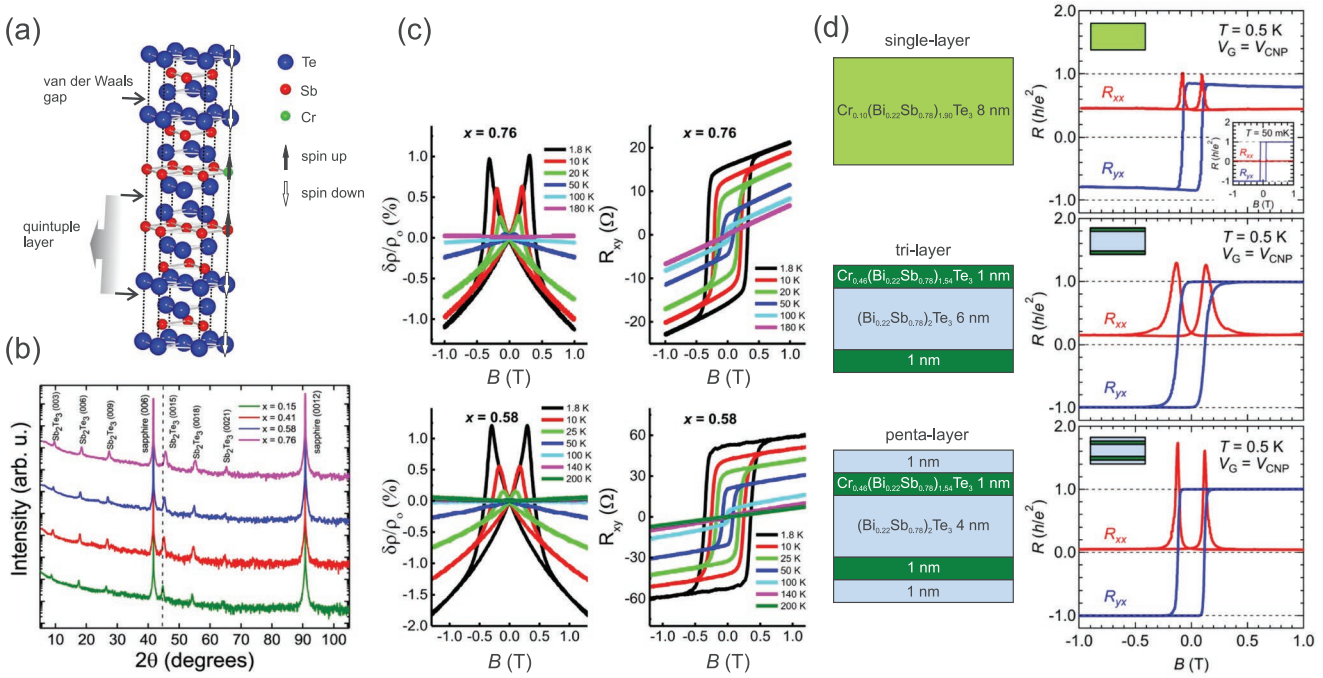

Figure 6. Cr-doped TI single-layer films and heterostructures. a) Crystal structure of Sb_2Te_3 with substitutional Cr doping (on Sb sites). The spin orientations of the individual elements were determined using XMCD. b) Out-of-plane XRD spectra of $Cr_xSb_{2-x}Te_3$ films for several Cr doping concentrations. c) Temperature-dependent transport results for $Cr_xSb_{2-x}Te_3$ films ($x = 0.58$ [below] and 0.76 [above]). Left: longitudinal resistance versus magnetic field; right: Hall resistance versus magnetic field. d) Transport results (at 0.5 K) for a Cr:BST single-layer (top), a modulation-doped trilayer (middle), and a pentatuple layer (bottom) structure (in which the second type of layer is undoped BST). The QAHE was observed in all films, but up to different temperatures. Insert in the top panel: transport results of the single-layer film at 50 mK. a) Adapted under the terms of the CC-BY Creative Commons Attribution 4.0 International license (https://creativecommons.org/licenses/by/4.0).[93] Copyright 2017, American Physical Society. b,c) Adapted under the terms of the CC-BY Creative Commons Attribution 4.0 International license (https://creativecommons.org/licenses/by/4.0).[144] © Copyright 2018, The Authors, published by Springer Nature. d) Reproduced with permission.[30] Copyright 2015, AIP Publishing.

is fully quantized at 50 mK (see inset) and decreases to $0.8h/e^2$ when the temperature rises to 0.5 K, at which the QAHE is still preserved in the heterostructure samples. This is because, in the heterostructure films, 1 nm-thick heavily-doped Cr:BST layers induce a large-bandgap due to the high Cr concentration, while the edge conduction in the surface states is preserved due to the reduced impurity scattering. The QAHE temperature of the pentalayer film is therefore increased to 2 K through the separation of magnetic dopants and surface conduction channels.

4.2. Magnetic-Insulator/Topological-Insulator Heterostructures

Since magnetic dopants inevitably introduces defects to the surface states of a single-layer TI film, magnetic proximity coupling has been raised as an alternative approach to break the time-reversal symmetry while maintaining the TI surface free from impurities.[27,28] Magnetic insulators such as EuS have Curie temperatures above the mK range and their insulating nature keeps them away from interfering quantum conductance in MI/TI heterostructures.[170,181–184] EuS films with a T_C of ≈17 K have an in-plane magnetic easy axis, yet there are hints that the magnetic moments are canted at the interface of EuS/Bi_2Se_3 heterostructures.[146,185] Based on PNR measurements, Katmis et al. claimed the existence of interfacial ferromagnetism in EuS/Bi_2Se_3, with the magnetic ordering extending up to 2 nm into the Bi_2Se_3 layer.[186] This short-range ferromagnetism was still observable at room temperature despite the low T_C of EuS, which is very peculiar and was argued to be due to the strong SOC from the surface of Bi_2Se_3. In another study of EuS/Bi_2Se_3, Lee et al. found both in-plane and out-of-plane ferromagnetic moments using magnetic second-harmonic generation.[187] Both claims have been challenged by a more recent XMCD study of EuS/Bi_2Se_3 and EuS/BST, in which neither significant induced magnetism in the TIs nor an enhancement of the magnetic moment of Eu near the interface was found.[188] In fact, the induced magnetic moments were below the typical XMCD detection limit of ≈10^{-3} μ_B for these materials (see Supporting Information in ref. [188]).

Apart from EuS, interfacial magnetism has been studied in TIs in proximity to other MI materials, such as $Tm_3Fe_5O_{12}$ (TIG),[90,189,190] $Y_3Fe_5O_{12}$ (YIG),[148,191–197] $Cr_2Ge_2Te_6$,[198–200] and $BaFe_{12}O_{19}$.[201,202] Tang et al. observed an robust AHE in BST films at 400 K which were proximity-coupled to TIG, a ferrimagnetic insulator material with a T_C of 560 K.[90] The magnetic interaction in TIG is through superexchange leading to antiferromagnetic coupling between Fe moments. **Figures 7**a and 7b show the schematic of the BST/TIG heterostructure studied by Tang et al. and its corresponding band structure, respectively. The TIG layer is grown on a substituted gadolinium gallium garnet (SGGG) substrate, so it experiences tensile strain which helps to establish out-of-plane anisotropy, breaking the TRS in

the BST layer and inducing an exchange gap (Δ_{ex}) in its surface states. Smooth interfaces are found in the BST/TIG film without visible defects or secondary phases, as revealed by the cross-sectional TEM image (**Figure 7**c). Figure 7d,e shows the results of Hall resistance measurements in the BST/TIG heterostructures at 400 K with different Bi to Te ratios (x = 0.20 and 0.30 in $(Bi_xSb_{1-x})_2Te_3$). These ratios were chosen to tune the carrier type in BST by positioning the chemical potential just below (x = 0.20) and above (x = 0.30) the Dirac point, respectively, as indicated in the lower insert of the figures. The square-shaped hysteresis loops confirm the existence of out-of-plane ferromagnetic ordering in TIG/BST. Since TIG has a significantly larger resistivity than BST, and therefore contributes an insignificant number of carriers, the opposite polarities of the linear slope corresponds to the different carrier types in BST, that is, holes for x = 0.20 and electrons for x = 0.30. The longitudinal resistance of both films decreases monotonically as the temperature increases (see upper inset), matching the behavior of bulk semiconductors where the chemical potential resides in the bulk gap.

The ferrimagnetic insulator YIG that shares similar structural and magnetic properties to TIG. Che et al. produced Bi_2Se_3/YIG heterostructures with high crystallinity and abrupt interface (see Figure 7f for the cross-sectional HAADF-STEM image).[195] The schematics of the three films investigated are depicted in Figure 7g. Apart from the main Bi_2Se_3/YIG film marked as BS1, there are two other samples introduced in this study for reference: Bi_2Se_3/AlO_x/YIG (BS2) in which the interfacial coupling between MI and TI is suppressed by the insertion of an AlO_x layer, and Bi_2Se_3/GaAs (BS3) to verify if the origin of magnetization in BS1 is coming from YIG. Figure 7h shows the Hall resistance results for the three samples at 1.9 K before (lower insert) and after (main figure) subtraction of the linear background aligned at high fields, and the upper insert shows the measurement geometry of the Hall bars. The AHE becomes visible for the BS1 sample after background removal, proving the broken TRS in the heterostructure in an external magnetic field. In contrast, there is no sign of an AHE in the reference samples. A detailed temperature-dependent study was carried out for BS1, which reveals a gradual reduction of the AHE signal as the temperature is increased from 1.9 to 30 K (Figure 7i). This behavior is in contrast to the magnetic properties of bare YIG, for which an out-of-plane magnetic moment is found at 300 K as shown in the lower insert of Figure 7i.

It should be mentioned that a reciprocal effect has also been found in MI/TI heterostructures, that is, magnetism in an MI can also be significantly influenced by the interfacing of a TI. In a recent study of YIG/Bi_2Se_3 heterostructures,[197] the TSS in

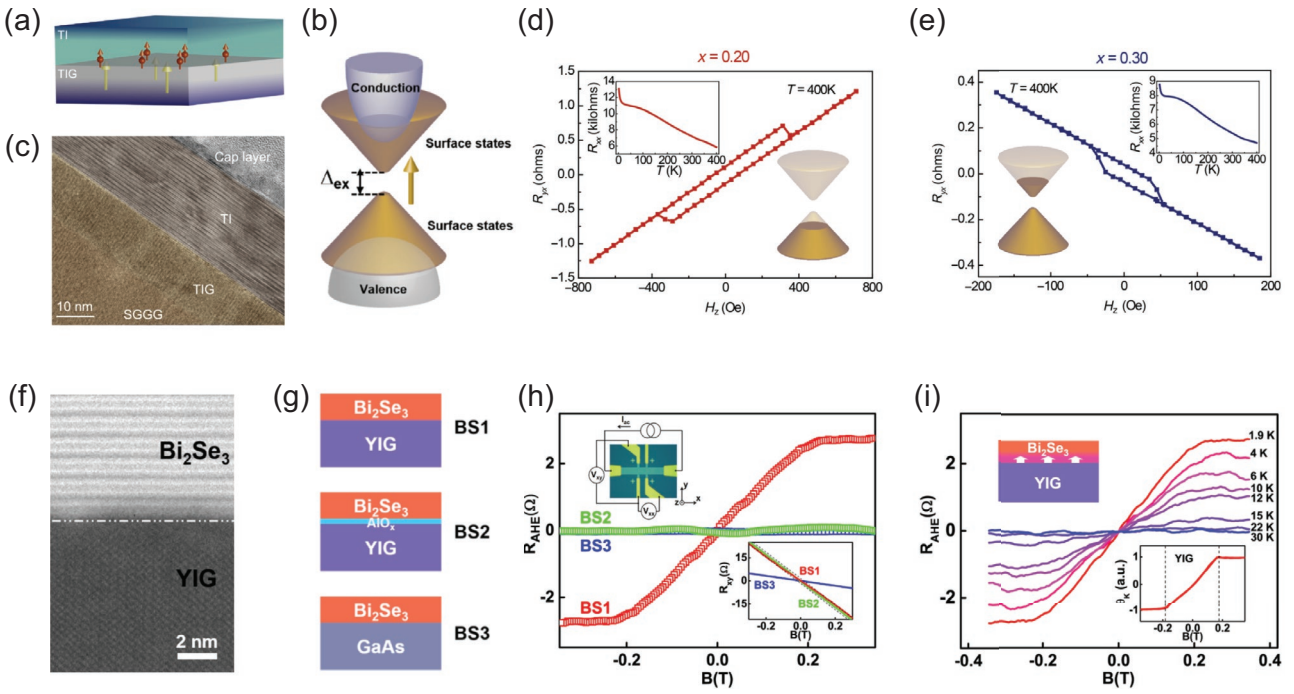

Figure 7. Magnetic-insulator/TI heterostructures: BST/TIG and Bi_2Se_3/YIG. a) Schematic of the TI/TIG heterostructure with spins pointing out-of-plane. b) Schematic showing the opening of the surface bandgap (Δ_{ex}) due to exchange interaction. c) Cross-sectional HR-TEM image of the TIG/BST (20 QL) bilayer structure. d,e) Hall resistance of TIG/$(Bi_xSb_{1-x})_2Te_3$ (5 QL) at 400 K, with x = 0.20 and x = 0.30, respectively. Upper insert: temperature dependence of the longitudinal resistance of the film. Lower insert: schematic illustrating the chemical potential of the surface state. f) Cross-sectional HAADF-STEM image of the YIG/Bi_2Se_3 bilayer structure. g) Schematic showing the layered structures of three different YIG/Bi_2Se_3 films, marked as BS1, BS2, and BS3, respectively. h) Hall resistance of the three YIG/Bi_2Se_3 films at 1.9 K, after subtracting the linear background. Upper insert: geometry of the electrical transport measurements. Lower insert: Hall resistance results before subtracting the linear background. i) Hall resistance of BS1 at different temperatures. Upper insert: schematic of the bilayer film demonstrating interfacial exchange. Lower insert: magnetization of the YIG film at 300 K measured by polar MOKE. a–e) Adapted with permission.[90] Copyright 2017, The Authors, published by American Association for the Advancement of Science. Reprinted/Adapted from ref. [90] © The Authors, some rights reserved; exclusive licensee American Association for the Advancement of Science. Distributed under a CC BY-NC 4.0 license. f–i) Adapted with permission.[195] Copyright 2018, American Chemical Society.

Bi_2Se_3 can produce a perpendicular magnetic anisotropy, which results in a decrease in the gyromagnetic ratio and enhancement of the damping in YIG. This new approach of controlling magnetism of ferromagnetic layers through proximity to TIs is worth further investigations.

Despite the success of establishing short-range magnetic order and independently tuning the electronic and magnetic properties of TI layers,[193] the Hall resistances demonstrated in most MI/TI heterostructures are still far from the quantum regime. One possible explanation of this shortcoming is the weak exchange interaction between the MI and the TI layer due to their distinctly different lattice structures, resulting in a small bandgap in the topological surface states. It is worth noting the exceptional case of (Zn,Cr)Te/BST/(Zn,Cr)Te, a MI/TI/MI system in which the QAHE was demonstrated at 0.1 K,[32] resulting from the strong exchange coupling between the Te atoms in (Zn,Cr)Te and BST, and the smooth interfaces between these lattice-matched layers. It is therefore desirable to improve the design of TI heterostructures to combine materials with similar structural properties in adjacent layers, one example being the rare-earth-doped TI superlattice systems described in the next section.

4.3. Rare-Earth-Doped Single-Layer Films and Heterostructures

It is known that the bandgap size of the topological surface states is proportional to the magnetic moment in MTI films. So far, all QAH insulators have been doped with transition metal elements with an atomic moment of less than, or on the order of (for Cr), 3 μ_B. To overcome the dilemma of small bandgap (low doping scenario) and large surface disorder (high doping scenario), RE elements with large atomic moments have been considered as alternative dopants to raise the QAHE temperature.[203] Although there is still no evidence of QAHE, novel electronic and magnetic properties have been demonstrated in RE-doped TIs. For instance, Gd-doped $(Bi,Sb)_2(Te,Se)_3$ was found to transform from a paramagnetic to antiferromagnetic phase upon cooling, a phenomenon explained by Gd–Gd exchange coupling through Te ions.[127,204,205] Sm-doped Bi_2Se_3 which can exhibit ferromagnetism up to 52 K[206] has also been proposed as a possible magnetic axion insulator system to realize chiral hinge states and surface QAHE.[207]

We grew Bi_2Te_3 thin films doped with Ho, Gd, or Dy, and confirmed good crystal structure with substitutional doping in all films, with a RE concentration of up to $x = 0.355$ in the form of $(RE_xBi_{1-x})_2Te_3$.[80–82,84,116,126,208] Using SQUID magnetometry, we have found that all the $(RE_xBi_{1-x})_2Te_3$ films investigated are paramagnetic (**Figure 8**a). While the atomic moments of RE elements in$(Ho_xBi_{1-x})_2Te_3$ and $(Gd_xBi_{1-x})_2Te_3$ films are independent of doping concentration, a monotonic increase in the atomic moment is observed in $(Dy_xBi_{1-x})_2Te_3$ following the decreasing doping, reaching up to 12.6 μ_B in the lowest doped film ($x = 0.046$),[81] which is shown in Figure 8b. This may be explained by antiferromagnetic ordering in highly doped Dy:Bi_2Te_3 reminiscent of elemental Dy.[209] Interestingly, despite the absence of ferromagnetic ordering, a gap opening was observed in $(Dy_{0.113}Bi_{0.887})_2Te_3$ using ARPES at both low temperature and room temperature,[83] while the surface Dirac point was found to preserve in Ho- and Gd-doped films.[80,116] Figure 8c shows the band structure and energy distribution curve of $(Dy_{0.113}Bi_{0.887})_2Te_3$ along the Γ–K direction. A gap opening can be found at the Dirac point (indicated with arrow) of the linear-dispersed surface band, which is also reflected as a local intensity peak in the energy distribution curve. Meanwhile, the surface band of $(Dy_{0.055}Bi_{0.945})_2Te_3$ is gapless (not shown here), similar to Ho- and Go-doped films. Further, inhomogeneous and short-ranged ferromagnetic patches have been revealed in Dy:Bi_2Te_3 surrounded by a paramagnetic matrix, indicating the possibility of establishing magnetic order by proximity coupling to FM layers.[86]

Following the experimental results listed above, we designed a magnetic TI superlattice system with alternating transition metal and rare earth doping, that is, [CST/DBT].[87] XMCD measurements were applied to the superlattice in order to probe the magnetism in a element-specific way. Figure 8d shows the Arrott plots of the XMCD peak asymmetries at Cr L_3 (in TEY) and Dy M_5 (in LY) edges. By producing a linear fit at the high magnetic field region, we find ferromagnetic order at remanence in both CST and DBT layers of the sample, with a Curie temperature of 70 and 17 K, respectively. First-principles calculations demonstrate that ferromagnetism extends over several atomic layers from the interfaces into DBT, which originates from strong antiferromagnetic coupling between Cr and Dy across the interface. The predicted Curie temperature of the DBT layers is 23 K, in good agreement with the experimental results. Due to the limitation of XMCD itself that is either sensitive only to the surface or the entire film stack, we also carried out PNR measurements to layer-resolve the magnetic profile of another [CST/DBT] superlattice sample.[86] The PNR results are shown in Figure 8e, with an in-plane external field applied at 3 and 30 K. Through developing a model that best fits the experimental data under a field of 0.65 T (top and middle panels of Figure 8e), we find that magnetization of the superlattice looks homogeneous throughout individual layers without apparent interfacial effects. Another PNR measurement under a small field of 0.02 T (bottom panel of Figure 8e) demonstrated small but existent net moment in Dy-doped layers, indicating that a complex spin arrangement may be present, such as antiferromagnetic order or twisted spin structures. Finally, we have also discovered exchange bias effect in the [CST/DBT] superlattice system,[210] which will be discussed in detail in the following section.

4.4. Exchange-Biased Heterostructures

The exchange bias effect reveals itself as a horizontal shift in magnetic hysteresis loops after field-cooling (FC).[211] Exchange bias has been found in many FM/AF heterostructures, as the spins of the FM layer close to the interface are pinned by the AF layer via the exchange interaction, changing the magnitude of external field required to complete a magnetization reversal. Further, extra uniaxial anisotropy has been identified in several ferromagnetic materials due to the exchange coupling to antiferromagnets, resulting in an increased T_C of the ferromagnetic layer.[212–214] He et al. demonstrated exchange bias in $[CST/CrSb]_n$ superlattices,[215] in which antiferromagnetic CrSb is well

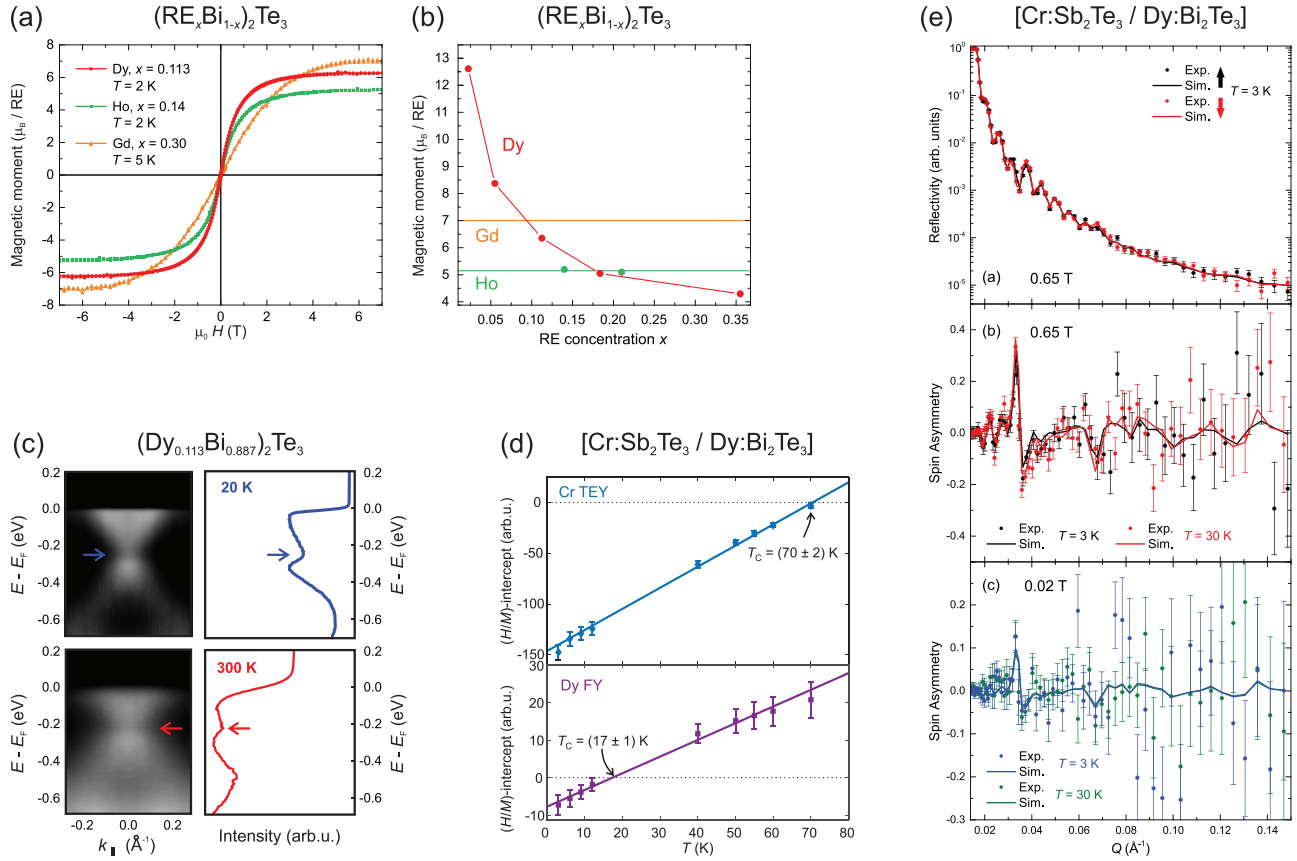

Figure 8. Rare-earth-doped MTIs. a) Out-of-plane magnetometry results of the $(RE_xSb_{1-x})_2Te_3$ films, with RE = Dy, Ho, or Gd. b) Atomic magnetic moment of the RE dopants in the $(Re_xSb_{1-x})_2Te_3$ films with different doping concentrations. c) ARPES results for a $(Dy_{0.113}Bi_{0.887})_2Te_3$ thin film, showing the band structures along the K–Γ–K direction (left) and energy distribution curves (right), at 20 and 300 K, respectively. The locations of Dirac point are indicated by arrows. d) Arrott plots extracted from XMCD results of a [CST/DBT] superlattice sample. The XMCD peak asymmetry of the Cr L_3 and Dy M_5 edges are obtained in TEY and LY modes, respectively. e) PNR data and associated fits of another [CST/DBT] superlattice sample with an in-plane magnetic field. Top: reflectivity curve for spin-up and spin-down neutrons at 3 K in a field of 0.65 T; middle/bottom: spin asymmetries at 3 and 30 K in a field of 0.65 and 0.02 T, respectively. a,b) Reproduced with permission.[203] Copyright 2019, Wiley VCH. c) Adapted under the terms of the CC-BY Creative Commons Attribution 4.0 International license (https://creativecommons.org/licenses/by/4.0).[83] Copyright 2015, The Authors, published by Springer Nature. d) Reproduced with permission.[87] Copyright 2018, The American Physical Society. e) Adapted with permission.[88] Copyright 2019, The American Physical Society.

lattice-matched to CST, allowing for the growth of high-quality epitaxial CST films. Proximity coupling to CrSb modulates the spin textures in CST close to the interface, and elevates its T_C monotonically from 40 to 90 K when $[CST/CrSb]_n$ is stacked up from $n = 0$ (only CST layer) to $n = 10$. Apart from CrSb, antiferromagnetic Cr_2O_3 is also lattice-matched to the $(Bi,Sb)_2(Te,Se)_3$ family. Wang et al. found that by increasing the thickness of the Cr_2O_3 layer from 1 to 35 unit cells (1 unit cell is ≈1.36 nm thick), the T_C of CST/Cr_2O_3 heterostructures increases from 39 to 50 K compared to the CST single-layer film.[216] In addition, due to the competition between the Zeeman energy of the Cr_2O_3 layer and the antiferromagnetic coupling energy between CST and Cr_2O_3, both positive and negative exchange bias can be demonstrated in CST/Cr_2O_3 heterostructures, by tuning the magnitude of the external magnetic field during the cooling process. Recently, both exchange bias and the QAHE have been realized in a CST/Cr_2O_3 system.[33] The QAHE temperature was 20 mK and only positive exchange bias was observed in the system.

Exchange bias has also been demonstrated in $[CST/DBT]_{10}$ superlattices.[210] Using HAADF-STEM, abrupt interfaces and constant layer thicknesses throughout the stack were confirmed (**Figure 9**a). Figure 9b shows the hysteresis loops of $[CST/DBT]_{10}$ measured at 1.8 K after out-of-plane field cooling from room temperature. Clearly, positive-field-cooling (PFC, in orange) and negative-field-cooling (NFC, in purple) induces loop shifts towards the opposite direction. The hysteresis recorded after zero-field-cooling (ZFC, in black) is also demonstrated as a reference, showing no sign of a horizontal shift. The exchange bias field (H_{EB}), defined as the shift of the center of the loop from the unbiased case, decreases monotonically from 0.08 T at 1.8 to 0 at 100 K (Figure 9c). This finding is rather unexpected in the [CST/DBT] system as DBT itself is paramagnetic instead of antiferromagnetic.[86] In order to understand the microscopic origin of the exchange-biased magnetic response, density functional theory calculations were carried out showing that when $[CST/DBT]_{10}$ is positive-field-cooled, the most stable spin configuration of the Cr-Dy-Dy chain at the

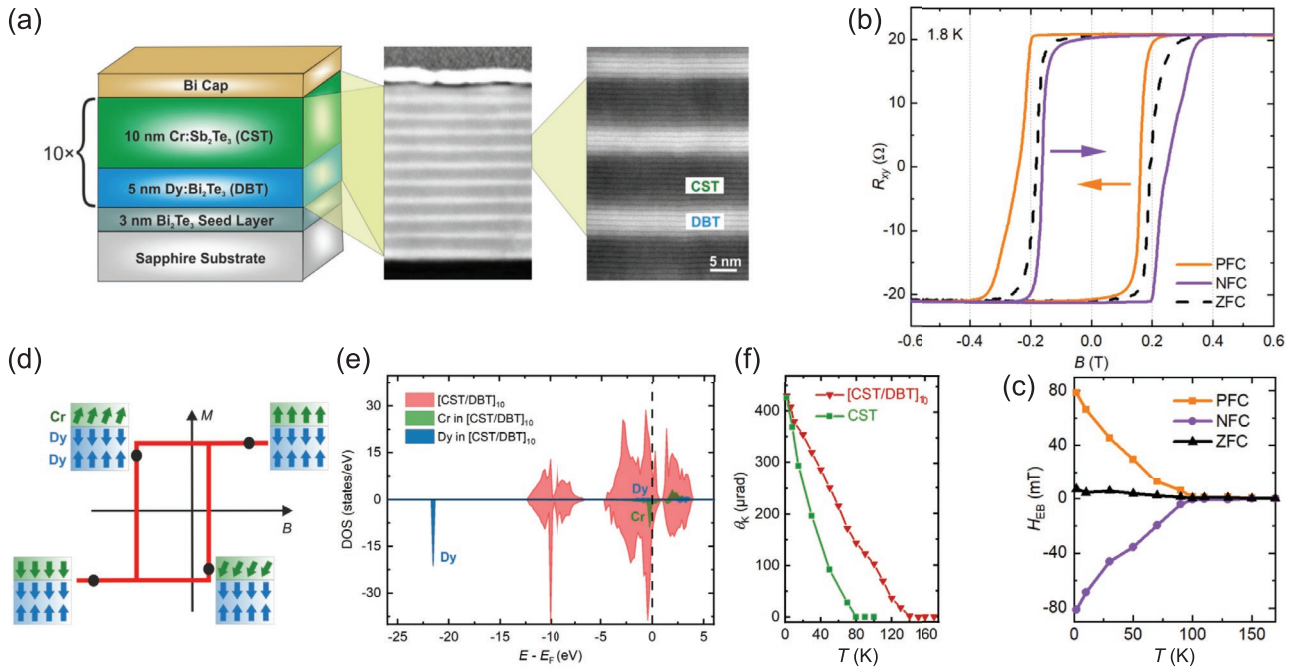

Figure 9. Exchange-biased $[CST/DBT]_{10}$ superlattice. a) Schematic and cross-sectional HAADF-TEM images of the $[CST/DBT]_{10}$ superlattice. b) Exchange-biased hysteresis loops of the superlattice measured at 1.8 K, after positive-field-cooling (PFC), negative-field-cooling (NFC), and zero-field-cooling (ZFC) from room temperature. c) Temperature-dependent exchange bias field of the superlattice. d) Schematic of the spin configurations at the Cr/Dy interface after PFC. e) Density-of-states of the interfacial Cr-Dy-Dy chain in the "up–down–up" configuration. f) Temperature-dependent magnetization of the $[CST/DBT]_{10}$ superlattice and CST single-layer film. Adapted under the terms of the CC-BY Creative Commons Attribution 4.0 International license (https://creativecommons.org/licenses/by/4.0).[210] Copyright 2020, The Authors, published by American Chemical Society.

interface is the "up–down–up" configuration. Figure 9d depicts the interfacial spin configurations of Cr-Dy-Dy in a hysteresis loop after PFC. The calculation therefore indicates possible antiferromagnetic ordering in DBT induced by proximity coupling to CST at the interface. The density-of-states of the Cr-Dy-Dy chain in the "up–down–up" configuration is shown in Figure 9e. The distribution of Cr states is mainly concentrated at around E_F, while Dy states mostly reside at –22 eV, indicating Cr dopants contribute carriers and increase the conductivity of the film, whereas Dy dopants have a marginal effect on the conductivity. This finding echoes the high-resistivity that was found in DBT single-layer films.[210] Further, as illustrated in Figure 9f, by comparing the temperature-dependent magnetization, an increase of T_C by 60 K was observed in the $[CST/DBT]_{10}$ superlattice (T_C = 140 K, in red), compared to a CST single-layer film (T_C = 80 K, in green) grown under the same conditions.

Based on the examples illustrated above, exchange-biased heterostructure engineering can be a promising route to increase the magnetic ordering temperature of MTI films without decreasing their crystalline quality, and various QAH insulators, such as Cr-doped and V-doped BST, are encouraging choices for the integration into advanced MTI/AF systems. Apart from ferromagnetic TI films, the anomalous Hall and exchange bias effects have also been observed in undoped BST films in proximity to antiferromagnetic MnTe. Seeding of topological charges was found in BST/MnTe heterostructures which was ascribed to interfacial spin pinning,[217] leading to the topological Hall effect in electrical transport. When first observed, the THE was considered as being intimately connected to chiral spin textures in real space, such as magnetic skyrmions,[218] as will be discussed in detail in the next section.

4.5. Magnetic Skyrmions and Topological Hall Effect

Magnetic skyrmions are small, concentric whirls of gradually canting spins, which can be regarded as quasiparticles originating from topological defects in real space.[219] Depending on their symmetry, most skyrmions can be categorized into two types shown in **Figure 10**a: Bloch-type skyrmions with a swirl, which can be clockwise or counter-clockwise, and Néel-type skyrmions in which the in-plane component of the spins is either pointing towards the center or away from it. Skyrmions can be as small as some nanometers in diameter, dictated by the strength of the symmetric exchange interaction, the antisymmetric Dzyaloshinskii–Moriya interaction (DMI), and the anisotropy of a material.[220] They can be created, translated and annihilated, making them ideal candidates for, for example, racetrack memory,[221] radio-frequency devices,[222] logic gate devices,[223] and magnonic crystal applications.[224] The DMI, which is a prerequisite for the formation of skyrmions, arises from strong SOC. Considering that strong SOC is also a fundamental materials requirement for TIs, it is not entirely surprising that skyrmions may also be observed in TI heterostructures.

In fact, skyrmionium (a composite skyrmions with a double-twisted core) has been observed in NiFe/CST heterostructures,[165] where the NiFe film was grown as a wedge, allowing

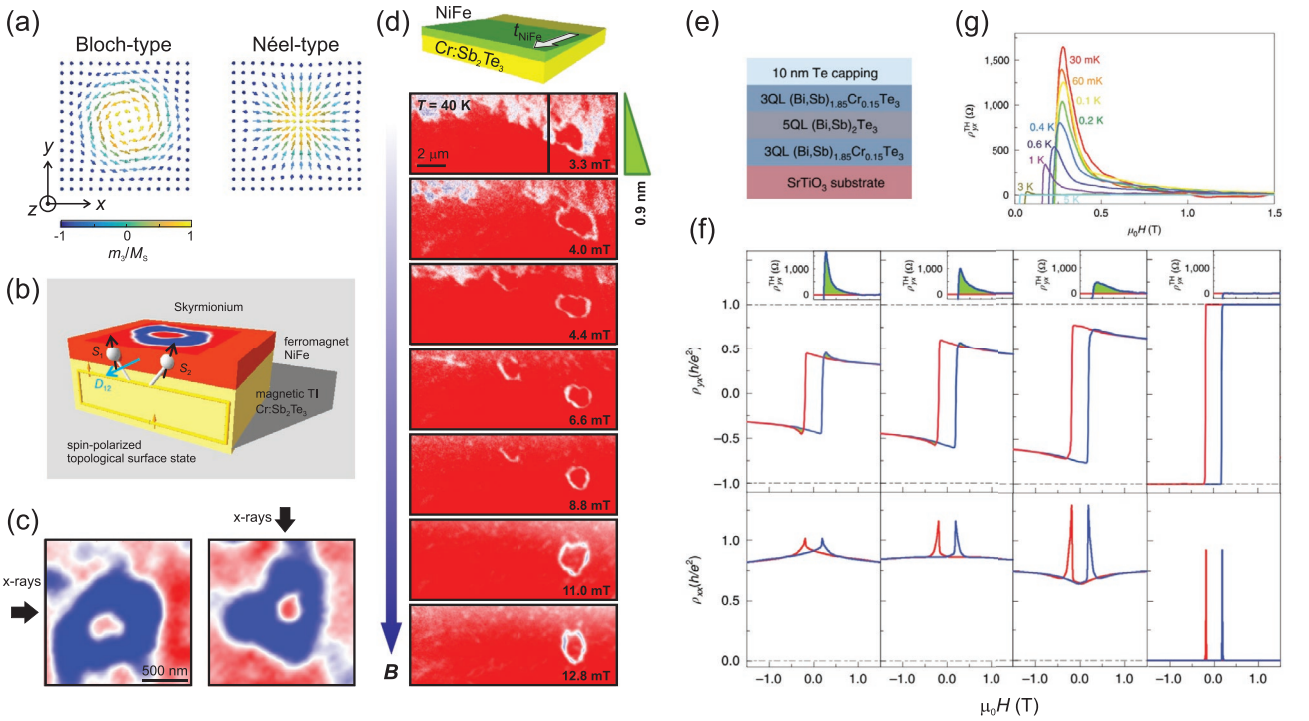

Figure 10. Magnetic skyrmions and topological Hall effect in MTI heterostructures. a) Schematic showing the two most common types of magnetic skyrmions: Bloch- (left) and Néel-type skyrmions (right). b) Schematic of the NiFe/CST heterostructure, illustrating a skyrmionium in the NiFe layer, the origin of the DMI, and the connection with topological surface states in the CST layer. c) Skyrmionium mapped by XPEEM at 44 K with the X-ray energy tuned to the Fe L_3 absorption edge. The X-rays were incident from two perpendicular directions. d) XPEEM results showing the creation and manipulation of skyrmionium by applying an out-of-plane field in a wedge-shaped NiFe film on CST. e) Schematic of the CST/BST/CST structure in which both the QAHE and THE occur at the same time. f) Transport results of the CST/BST/CST structure at 30 mK obtained with different gate voltages. Top: zoom-in of the THE-hump (shaded in green); middle: Hall resistance versus applied field; bottom: longitudinal resistance versus applied field. g) Zoom-in of the THE-hump at different temperatures. b–d) Adapted with permission.[165] Copyright 2018, American Chemical Society. e–g) Reproduced with permission.[232] Copyright 2020, The Authors, published by Springer Nature.

for the convenient imaging of the thickness dependence of skyrmionium formation. Figure 10b shows the schematic of the heterostructure, illustrating the presence of interfacial DMI and the topological surface state in the TI layer. Using XPEEM mapping at the Fe L_3 absorption edge, it is clear that skyrmionium solely forms in the NiFe layer, however, only below the Curie temperature of CST, indicating an intimate relationship between the real-space spin texture and the ferromagnetic ordering of the MTI layer. Figure 10c shows an XPEEM image of an isolated skyrmionium, with X-rays incident from different directions. Further, skyrmionium was only observable at an intermediate thickness range of the NiFe layer, where NiFe is thick enough to establish long-range magnetic order, yet thin enough to have proximity coupling dominating over the demagnetization energy. The formation of skyrmionium can also be manipulated by applying an external magnetic field. By gradually increasing the out-of-plane field from 0 to 12.8 mT, individual skyrmioniums can be generated and moved away from the sample edge, with variable diameters at different field magnitudes (see Figure 10d for detail).

As was mentioned in the previous section, the THE was observed in exchange-biased BST/MnTe heterostructures.[217] Revealing itself as an additional hump in the Hall resistance usually around the magnetization reversal, the THE is a transport signature tied to non-trivial spin textures such as magnetic skyrmions. This hump originates from the extra scattering factor to the conduction carriers induced by an emergent magnetic field from skyrmions.[225] Apart from BST/MnTe, the THE has also been found in Mn-doped Bi_2Te_3 films,[226] Cr:BST/BST,[227] Cr_2Te_3/Bi_2Te_3,[228] $BaFe_{12}O_{19}/Bi_2Se_3$,[229] GdFeO/BST,[230] and $Sb_2Te_3/V:Sb_2Te_3$ heterostructures.[231] Recently, the concurrence of both QAHE and THE was realized in Cr:BST/BST/Cr:BST sandwich structures (schematic shown in Figure 10e).[232] Figure 10f shows the Hall resistance (middle panel) and longitudinal resistance (bottom panel) of the film at 30 mK with different bottom gate voltages (V_g): i) –220 V, ii) –140 V, iii) –100 V, iv) 0 V. When $V_g < 0$, extra humps (shaded in green) can be found in the loops, and a zoom-in of this THE feature is illustrated in the top panel. Further, the QAHE is realized in the film when $V_{gg} = 0$. The size of the THE hump decreases monotonically with increasing temperature and disappears at 5 K (Figure 10g).

It should also be noted that the observation of the THE alone does not conclusively prove the presence of magnetic skyrmions, as has been pointed out in several studies.[233–239] This is because the ferromagnetism in different parts of a sample, for example, surface and bulk, may have different coercivities and temperature dependencies, such that the combined hysteresis loop can have humps mimicking a skyrmion-induced topological Hall signal.[240,241] It is therefore important not to solely rely

on transport measurements to probe skyrmions in magnetic films, but to conduct supporting measurements by, that is, resonant soft X-ray scattering for ordered systems or real-space magnetic imaging for individual skyrmions.[242–245]

5. Conclusions and Perspectives: $MnBi_2Te_4$ and Beyond

We have given a broad overview of different aspects of magnetic topological insulator heterostructures, covering their growth and structure, their electronic and magnetic properties and most common characterization techniques, followed by an illustration of QAH insulators, MI/TI heterostructures, RE-doped TI materials, exchange-biased heterostructures, and heterostructures hosting skyrmions or showing the THE. The synthesis of heterostructures provides the freedom to design materials for use at the quantum limit, such as the QAH insulator state or the magnetoelectric effect, especially in terms of material choice, thickness control and interface engineering. The fast-paced advancement of materials growth, device fabrication, and theoretical studies will further promote the field of topological condensed matter physics in the form of MTI heterostructures and beyond.

The prerequisites for QAH insulators are: i) a strong SOC that leads to the formation of linearly dispersing surface states, and ii) magnetic order that induces a gap at the Dirac point. In terms of materials properties, these are contradicting requirements: Strong SOC is favored by heavy elements, while high temperature magnetic order is commonly found in systems made of light 3d elements. Both magnetic doping and heterostructure engineering of BST films were adapted to resolve this issue, nevertheless room temperature QAH insulators are still nowhere in sight, begging the question if there is a way to optimize heterostructures further. The new QAH insulator $MnBi_2Te_4$ was designed in the spirit of combining strong SOC with magnetic ordering in a single, intrinsic MTI.[246] The ternary van der Waals compound $MnBi_2Te_4$ consists of Te–Bi–Te–Mn–Te–Bi–Te septuple layers, which can be viewed as a Bi_2Te_3 quintuple layer with an intercalated Mn–Te bilayer. While Mn–Te orders ferromagnetically in the plane, neighboring planes couple antiferromagnetically across septuple layers. Most importantly, in zero applied field, the overall behavior is antiferromagnetic for an even number of septuple layers, and ferromagnetic for an odd number.[35,247] The theoretically predicted topologically non-trivial behavior of $MnBi_2Te_4$ was first experimentally confirmed through XMCD, ARPES, and electron spin resonance experiments in 2019,[18] followed by a number of complementary studies that same year.[246,248–252] Following this series of groundbreaking discoveries, the zero-field QAHE was successfully realized in 5-SL $MnBi_2Te_4$ flakes at 1.4 K, which were exfoliated from a single crystal.[35] On the other hand, in 6-SL $MnBi_2Te_4$, the QAH insulator state was found above 9 T, while at zero field, a robust axion insulator state was reported.[253]

A controversial aspect of $MnBi_2Te_4$ remains the band structure of its topological surface state. There have been significant differences in surface bandgap sizes observed in ARPES experiments, ranging from 50 meV to hundreds of meV.[18,96,99,250,252] Moreover, there are also ARPES studies finding that the surface Dirac cone is gapless,[189,255,256] with no observable dependence on the temperature variation even across the antiferromagnetic-to-paramagnetic phase transition at 25 K. This phenomenon may be explained by the possible presence of magnetic domains at the surface.[189]

On the basis of the discovery of the QAH insulator $MnBi_2Te_4$, alternating stacks of Bi_2Te_3 and $MnBi_2Te_4$ have been grown to form superlattice $(MnBi_2Te_4)_m(Bi_2Te_3)_n$, for example, $MnBi_4Te_7$ ($m = 1$, $n = 1$) and $Mn_2Bi_6Te_{10}$ ($m = 1$, $n = 2$).[96,257,258] Eventually, the QAHE has been found in the bulk single crystal of $MnBi_2Te_4/(Bi_2Te_3)_4$ superlattice,[36] which has a ferromagnetic ground state in contrast to AF-ordered $MnBi_2Te_4$. Through high-energy electron irradiation and afterwards thermal annealing, a uniform distribution of donor vacancies is created to counterbalance the n-type carriers and then the surface bands are uplifted relative to the bulk bands, resulting in the QAHE and an elevated temperature.

Apart from stacking $MnBi_2Te_4$ with Bi_2Te_3 QLs, proximity coupling to 2D magnetic materials has also been proposed as a possible solution, such as $CrI_3/MnBi_2Te_4$ with possible exchange bias[259] (CrI_3 is one of the first confirmed 2D ferromagnets in the family of van der Waals materials[260]). We anticipate many more theoretical and experimental studies to be devoted to $(MnBi_2Te_4)_m(Bi_2Te_3)_n$ and heterostructures involving the fast-growing family of 2D magnetic materials.[261]

Over the recent years, comprehensive catalogs of topological materials have been compiled with the help of first-principles calculations to guide the search for new materials.[262–264] A vast variety of MTI single crystals, thin films, and proximity-coupled heterostructures have been predicted to yield exciting physics that are waiting to be synthesized. Regarding the currently used MTI materials, such as Cr:BST, further advancements in sample growth are needed to achieve uniform doping, and carefully designed measurement schemes are required to enable technological applications as low-dissipation spintronic devices. Beyond MTIs, new classes of quantum materials have appeared on the horizon,[266] such as twisted 2D layered crystals, topological semimetals, and ultrathin layered superconductors, which may provide intriguing solutions for current and future challenges in information technologies.

Acknowledgements

The authors would like to thank all of our colleagues who have contributed to our joint research efforts on topological insulators over the years (in alphabetical order): Crispin H. W. Barnes, David M. Burn, Adriana I. Figueroa, James S. Harris Jr., Barat Achinuq, Gerrit van der Laan, Sean Langridge, Vlado Lazarov, Stuart S. P. Parkin, Aakash Pushp, and Nina-J. Steinke. For the work presented in this review, the authors are particularly indebted to the graduate students Liam J. Collins-McIntyre, Alex A. Baker, Shilei Zhang, Piet Schönherr, Sarah E. Harrison, Liam B. Duffy, Angadjit Singh, and Ryuji Fujita. A special thanks goes to the John Fell Oxford University Press (OUP) Research Fund and RCaH, who have supported this work generously over the past 10 years. The Diamond Light Source, ISIS/STFC, the ESRF, BESSYII, ALBA, ILL, and PSI are acknowledged for many successful beamtimes. Finally, the authors acknowledge financial support from EPSRC (EP/M020517/1).

Conflict of Interest

The authors declare no conflict of interest.

Keywords

magnetic heterostructures, proximity effect, quantum anomalous Hall effect, topological insulators

Received: March 29, 2021
Revised: June 5, 2021
Published online: October 19, 2021

[1] M. N. Baibich, J. M. Broto, A. Fert, F. N. Van Dau, F. Petroff, P. Etienne, G. Creuzet, A. Friederich, J. Chazelas, *Phys. Rev. Lett.* **1988**, *61*, 2472.
[2] G. Binasch, P. Grünberg, F. Saurenbach, W. Zinn, *Phys. Rev. B* **1989**, *39*, 4828.
[3] P. A. Lee, N. Nagaosa, X.-G. Wen, *Rev. Mod. Phys.* **2006**, *78*, 17.
[4] K. v. Klitzing, G. Dorda, M. Pepper, *Phys. Rev. Lett.* **1980**, *45*, 494.
[5] Y. Zhang, Y.-W. Tan, H. L. Stormer, P. Kim, *Nature* **2005**, *438*, 201.
[6] M. Z. Hasan, C. L. Kane, *Rev. Mod. Phys.* **2010**, *82*, 3045.
[7] X.-L. Qi, S.-C. Zhang, *Rev. Mod. Phys.* **2011**, *83*, 1057.
[8] F. D. M. Haldane, *Phys. Rev. Lett.* **1988**, *61*, 2015.
[9] K. Ohgushi, S. Murakami, N. Nagaosa, *Phys. Rev. B* **2000**, *62*, R6065.
[10] C.-X. Liu, X.-L. Qi, X. Dai, Z. Fang, S.-C. Zhang, *Phys. Rev Lett.* **2008**, *101*, 146802.
[11] B. A. Bernevig, T. L. Hughes, S.-C. Zhang, *Science* **2006**, *314*, 1757.
[12] L. Fu, C. L. Kane, E. J. Mele, *Phys. Rev. Lett.* **2007**, *98*, 106803.
[13] J. E. Moore, L. Balents, *Phys. Rev. B* **2007**, *75*, 121306.
[14] X.-L. Qi, T. L. Hughes, S.-C. Zhang, *Phys. Rev. B* **2008**, *78*, 195424.
[15] H. Zhang, C.-X. Liu, X.-L. Qi, X. Dai, Z. Fang, S.-C. Zhang, *Nat. Phys* **2009**, *5*, 438.
[16] R.-L. Chu, J. Shi, S.-Q. Shen, *Phys. Rev. B* **2011**, *84*, 085312.
[17] G. Xu, J. Wang, C. Felser, X.-L. Qi, S.-C. Zhang, *Nano Lett.* **2015**, *15*, 2019.
[18] M. M. Otrokov, I. I. Klimovskikh, H. Bentmann, D. Estyunin, A. Zeugner, Z. S. Aliev, S. Gaß, A. U. B. Wolter, A. V. Koroleva, A. M. Shikin, M. Blanco-Rey, M. Hoffmann, I. P. Rusinov, A. Y. Vyazovskaya, S. V. Eremeev, Y. M. Koroteev, V. M. Kuznetsov, F. Freyse, J. Sánchez-Barriga, I. R. Amiraslanov, M. B. Babanly, N. T. Mamedov, N. A. Abdullayev, V. N. Zverev, A. Alfonsov, V. Kataev, B. Büchner, E. F. Schwier, S. Kumar, A. Kimura, L. Petaccia, G. Di Santo, R. C. Vidal, S. Schatz, K. Kißner, M. Ünzelmann, C. H. Min, S. Moser, T. R. F. Peixoto, F. Reinert, A. Ernst, P. M. Echenique, A. Isaeva, E. V. Chulkov, *Nature* **2019**, *576*, 416.
[19] X. Wu, J. Li, X.-M. Ma, Y. Zhang, Y. Liu, C.-S. Zhou, J. Shao, Q. Wang, Y.-J. Hao, Y. Feng, E. F. Schwier, S. Kumar, H. Sun, P. Liu, K. Shimada, K. Miyamoto, T. Okuda, K. Wang, M. Xie, C. Chen, Q. Liu, C. Liu, Y. Zhao, *Phys. Rev. X* **2020**, *10*, 031013.
[20] P. M. Perez-Piskunow, S. Roche, *Phys. Rev. Lett.* **2021**, *126*, 167701.
[21] R. Yu, W. Zhang, H.-J. Zhang, S.-C. Zhang, X. Dai, Z. Fang, *Science* **2010**, *329*, 61.
[22] C.-Z. Chang, J. Zhang, X. Feng, J. Shen, Z. Zhang, M. Guo, K. Li, Y. Ou, P. Wei, L.-L. Wang, Z.-Q. Ji, Y. Feng, S. Ji, X. Chen, J. Jia, X. Dai, Z. Fang, S.-C. Zhang, K. He, Y. Wang, L. Lu, X.-C. Ma, Q.-K. Xue, *Science* **2013**, *340*, 167.
[23] I. Lee, C. K. Kim, J. Lee, S. J. L. Billinge, R. Zhong, J. A. Schneeloch, T. Liu, T. Valla, J. M. Tranquada, G. Gu, J. C. S. Davis, *Proc. Natl. Acad. Sci. USA* **2015**, *112*, 1316.
[24] E. O. Lachman, A. F. Young, A. Richardella, J. Cuppens, H. Naren, Y. Anahory, A. Y. Meltzer, A. Kandala, S. Kempinger, Y. Myasoedov, M. E. Huber, N. Samarth, E. Zeldov, *Sci. Adv.* **2015**, *1*, e1500740.
[25] S. Grauer, S. Schreyeck, M. Winnerlein, K. Brunner, C. Gould, L. Molenkamp, *Phys. Rev. B* **2015**, *92*, 201304.
[26] M. Liu, W. Wang, A. R. Richardella, A. Kandala, J. Li, A. Yazdani, N. Samarth, N. P. Ong, *Sci. Adv.* **2016**, *2*, e1600167.
[27] A. Kandala, A. Richardella, D. W. Rench, D. M. Zhang, T. C. Flanagan, N. Samarth, *Appl. Phys. Lett.* **2013**, *103*, 202409.
[28] Y. Hou, J. Kim, R. Wu, *Sci. Adv.* **2019**, *5*, eaaw1874.
[29] C.-Z. Chang, W. Zhao, D. Y. Kim, H. Zhang, B. A. Assaf, D. Heiman, S.-C. Zhang, C. Liu, M. H. W. Chan, J. S. Moodera, *Nat. Mater.* **2015**, *14*, 473.
[30] M. Mogi, R. Yoshimi, A. Tsukazaki, K. Yasuda, Y. Kozuka, K. S. Takahashi, M. Kawasaki, Y. Tokura, *Appl. Phys. Lett.* **2015**, *107*, 182401.
[31] Y. Ou, C. Liu, G. Jiang, Y. Feng, D. Zhao, W. Wu, X.-X. Wang, W. Li, C. Song, L.-L. Wang, W. Wang, W. Wu, Y. Wang, K. He, X. Ma, Q. Xue, *Adv. Mater.* **2018**, *30*, 1703062.
[32] R. Watanabe, R. Yoshimi, M. Kawamura, M. Mogi, A. Tsukazaki, X. Z. Yu, K. Nakajima, K. S. Takahashi, M. Kawasaki, Y. Tokura, *Appl. Phys. Lett.* **2019**, *115*, 102403.
[33] L. Pan, A. Grutter, P. Zhang, X. Che, T. Nozaki, A. Stern, M. Street, B. Zhang, B. Casas, Q. L. He, E. S. Choi, S. M. Disseler, D. A. Gilbert, G. Yin, Q. Shao, P. Deng, Y. Wu, X. Liu, X. Kou, S. Masashi, X. Han, C. Binek, S. Chambers, J. Xia, K. L. Wang, *Adv. Mater.* **2020**, *32*, 2001460.
[34] M. Serlin, C. L. Tschirhart, H. Polshyn, Y. Zhang, J. Zhu, K. Watanabe, T. Taniguchi, L. Balents, A. F. Young, *Science* **2020**, *367*, 900.
[35] Y. Deng, Y. Yu, M. Z. Shi, Z. Guo, Z. Xu, J. Wang, X. H. Chen, Y. Zhang, *Science* **2020**, *367*, 895.
[36] H. Deng, Z. Chen, A. Wołoś, M. Konczykowski, K. Sobczak, J. Sitnicka, I. V. Fedorchenko, J. Borysiuk, T. Heider, Ł. Pluciński, K. Park, A. B. Georgescu, J. Cano, L. Krusin-Elbaum, *Nat. Phys.* **2021**, *17*, 36.
[37] H. J. Goldsmid, A. R. Sheard, D. A. Wright, *Br. J. Appl. Phys.* **1958**, *9*, 365.
[38] I. T. Witting, T. C. Chasapis, F. Ricci, M. Peters, N. A. Heinz, G. Hautier, G. J. Snyder, *Adv. Electron. Mater.* **2019**, *5*, 1800904.
[39] D. C. Mahendra, R. Grassi, J.-Y. Chen, M. Jamali, D. Reifsnyder Hickey, D. Zhang, Z. Zhao, H. Li, P. Quarterman, Y. Lv, M. Li, A. Manchon, K. A. Mkhoyan, T. Low, J.-P. Wang, *Nat. Mater.* **2018**, *17*, 800.
[40] Y. Li, Q. Ma, S. X. Huang, C. L. Chien, *Sci. Adv.* **2018**, *4*, eaap8294.
[41] E. Charles, E. Groubert, A. Boyer, *J. Mater. Sci. Lett.* **1988**, *7*, 575.
[42] G. Wang, L. Endicott, C. Uher, *Sci. Adv. Mater.* **2011**, *3*, 539.
[43] L. He, X. Kou, K. L. Wang, *Phys. Status Solidi RRL* **2013**, *7*, 50.
[44] T. P. Ginley, Y. Wang, S. Law, *Crystals* **2016**, *6*, 154.
[45] G. Zhang, H. Qin, J. Teng, J. Guo, Q. Guo, X. Dai, Z. Fang, K. Wu, *Appl. Phys. Lett.* **2009**, *95*, 053114.
[46] H. D. Li, Z. Y. Wang, X. Kan, X. Guo, H. T. He, Z. Wang, J. N. Wang, T. L. Wong, N. Wang, M. H. Xie, *New J. Phys.* **2010**, *12*, 103038.
[47] L. He, F. Xiu, Y. Wang, A. V. Fedorov, G. Huang, X. Kou, M. Lang, W. P. Beyermann, J. Zou, K. L. Wang, *J. Appl. Phys.* **2011**, *109*, 103702.
[48] J. Krumrain, G. Mussler, S. Borisova, T. Stoica, L. Plucinski, C. Schneider, D. Grützmacher, *J. Cryst. Growth* **2011**, *324*, 115.
[49] T. Guillet, A. Marty, C. Beigne, C. Vergnaud, M. T. Dau, P. Noel, J. Frigerio, G. Isella, M. Jamet, *AIP Adv.* **2018**, *8*, 115125.
[50] S. Kim, S. Lee, J. Woo, G. Lee, *Appl. Surf. Sci.* **2018**, *432*, 152.
[51] A. Richardella, D. M. Zhang, J. S. Lee, A. Koser, D. W. Rench, A. L. Yeats, B. B. Buckley, D. D. Awschalom, N. Samarth, *Appl. Phys. Lett.* **2010**, *97*, 262104.

[52] X. Liu, D. J. Smith, J. Fan, Y. Zhang, H. Cao, Y. P. Chen, B. J. Kirby, N. Sun, S. T. Ruggiero, J. Leiner, R. E. Pimpinella, J. Hagmann, K. Tivakornsasithorn, M. Dobrowolska, J. K. Furdyna, *AIP Conf. Proc.* **2011**, *1416*, 105.
[53] A. A. Taskin, S. Sasaki, K. Segawa, Y. Ando, *Phys. Rev. Lett.* **2012**, *109*, 066803.
[54] J. J. Lee, F. T. Schmitt, R. G. Moore, I. M. Vishik, Y. Ma, Z. X. Shen, *Appl. Phys. Lett.* **2012**, *101*, 013118.
[55] N. Bansal, Y. S. Kim, M. Brahlek, E. Edrey, S. Oh, *Phys. Rev. Lett.* **2012**, *109*, 116804.
[56] S. E. Harrison, S. Li, Y. Huo, B. Zhou, Y. L. Chen, J. S. Harris, *Appl. Phys. Lett.* **2013**, *102*, 171906.
[57] Y. Zhao, C.-Z. Chang, Y. Jiang, A. DaSilva, Y. Sun, H. Wang, Y. Xing, Y. Wang, K. He, X. Ma, Q.-K. X. Xue, J. Wang, *Sci. Rep.* **2013**, *3*, 3060.
[58] S. K. Jerng, K. Joo, Y. Kim, S. M. Yoon, J. H. Lee, M. Kim, J. S. Kim, E. Yoon, S. H. Chun, Y. S. Kim, *Nanoscale* **2013**, *5*, 10618.
[59] N. Bansal, M. R. Cho, M. Brahlek, N. Koirala, Y. Horibe, J. Chen, W. Wu, Y. D. Park, S. Oh, *Nano Lett.* **2014**, *14*, 1343.
[60] L. J. Collins-McIntyre, W. Wang, B. Zhou, S. C. Speller, Y. L. Chen, T. Hesjedal, *Phys. Status Solidi B* **2015**, *252*, 1334.
[61] S. Schreyeck, N. V. Tarakina, G. Karczewski, C. Schumacher, T. Borzenko, C. Brune, H. Buhmann, C. Gould, K. Brunner, L. W. Molenkamp, *Appl. Phys. Lett.* **2013**, *102*, 041914.
[62] X. Guo, Z. J. Xu, H. C. Liu, B. Zhao, X. Q. Dai, H. T. He, J. N. Wang, H. J. Liu, W. K. Ho, M. H. Xie, *Appl. Phys. Lett.* **2013**, *102*, 151604.
[63] O. Caha, A. Dubroka, J. Humlíček, V. Holý, H. Steiner, M. Ul-Hassan, J. Sánchez-Barriga, O. Rader, T. N. Stanislavchuk, A. A. Sirenko, G. Bauer, G. Springholz, *Cryst. Growth Des.* **2013**, *13*, 3365.
[64] F. Bonell, M. G. Cuxart, K. Song, R. Robles, P. Ordejon, S. Roche, A. Mugarza, S. O. Valenzuela, *Cryst. Growth Des.* **2017**, *17*, 4655.
[65] A. Koma, *Thin Sol. Films* **1992**, *216*, 72.
[66] X. Chen, X.-C. Ma, K. He, J.-F. Jia, Q.-K. Xue, *Adv. Mater.* **2011**, *23*, 1162.
[67] R. O. Carlson, *J. Phys. Chem. Solids* **1960**, *13*, 65.
[68] J. D. Keys, H. M. Dutton, *J. Appl. Phys.* **1963**, *34*, 1830.
[69] Y. C. Lan, D. Z. Wang, G. Chen, Z. F. Ren, *Appl. Phys. Lett.* **2008**, *92*, 101910.
[70] M. C. Shaughnessy, N. C. Bartelt, J. A. Zimmerman, J. D. Sugar, *J. Appl. Phys.* **2014**, *115*, 063705.
[71] Y. Xu, I. Miotkowski, C. Liu, J. Tian, H. Nam, N. Alidoust, J. Hu, C.-K. Shih, M. Z. Hasan, Y. P. Chen, *Nat. Phys.* **2014**, *10*, 956.
[72] L. J. Collins-McIntyre, S. E. Harrison, P. Schönherr, N.-J. Steinke, C. J. Kinane, T. R. Charlton, D. Alba-Veneroa, A. Pushp, A. J. Kellock, S. S. P. Parkin, J. S. Harris, S. Langridge, G. van der Laan, T. Hesjedal, *Europhys. Lett.* **2014**, *107*, 57009.
[73] Z. Zhou, Y.-J. Chien, C. Uher, *Phys. Rev. B* **2006**, *74*, 224418.
[74] L. Zhang, D. Zhao, Y. Zang, Y. Yuan, G. Jiang, M. Liao, D. Zhang, K. He, X. Ma, Q. Xue, *APL Mater.* **2017**, *5*, 076106.
[75] Z. Zhou, Y.-J. Chien, C. Uher, *Appl. Phys. Lett.* **2005**, *87*, 112503.
[76] J. Růžička, O. Caha, V. Holý, H. Steiner, V. Volobuiev, A. Ney, G. Bauer, T. Duchoň, K. Veltruská, I. Khalakhan, V. Matolín, E. F. Schwier, H. Iwasawa, K. Shimada, G. Springholz, *New J. Phys.* **2015**, *17*, 013028.
[77] L. J. Collins-McIntyre, L. B. Duffy, A. Singh, N.-J. Steinke, C. J. Kinane, T. R. Charlton, A. Pushp, A. J. Kellock, S. S. P. Parkin, S. N. Holmes, C. H. W. Barnes, G. van der Laan, S. Langridge, T. Hesjedal, *Europhys. Lett.* **2016**, *115*, 27006.
[78] A. Tcakaev, V. B. Zabolotnyy, R. J. Green, T. R. Peixoto, F. Stier, M. Dettbarn, S. Schreyeck, M. Winnerlein, R. C. Vidal, S. Schatz, H. B. Vasili, M. Valvidares, K. Brunner, C. Gould, H. Bentmann, F. Reinert, L. W. Molenkamp, V. Hinkov, *Phys. Rev. B* **2020**, *101*, 45127.
[79] P. P. J. Haazen, J.-B. Laloë, T. J. Nummy, H. J. M. Swagten, P. Jarillo-Herrero, D. Heiman, J. S. Moodera, *Appl. Phys. Lett.* **2012**, *100*, 082404.
[80] S. E. Harrison, L. J. Collins-McIntyre, S. L. Zhang, A. A. Baker, A. I. Figueroa, A. J. Kellock, A. Pushp, Y. L. Chen, S. S. P. Parkin, J. S. Harris, G. van der Laan, T. Hesjedal, *Appl. Phys. Lett.* **2015**, *107*, 182406.
[81] S. E. Harrison, L. J. Collins-McIntyre, S. L. Zhang, A. A. Baker, A. I. Figueroa, A. J. Kellock, A. Pushp, S. S. P. Parkin, J. S. Harris, G. van der Laan, T. Hesjedal, *J. Phys. Condens. Matter* **2015**, *27*, 245602.
[82] S. E. Harrison, L. J. Collins-McIntyre, S. Li, A. A. Baker, L. R. Shelford, Y. Huo, A. Pushp, S. S. P. Parkin, J. S. Harris, E. Arenholz, G. van der Laan, T. Hesjedal, *J. Appl. Phys.* **2014**, *115*, 023904.
[83] S. E. Harrison, L. J. Collins-McIntyre, P. Schönherr, A. Vailionis, V. Srot, P. A. van Aken, A. J. Kellock, A. Pushp, S. S. P. Parkin, J. S. Harris, B. Zhou, Y. L. Chen, T. Hesjedal, *Sci. Rep.* **2015**, *5*, 15767.
[84] A. I. Figueroa, A. A. Baker, S. E. Harrison, K. Kummer, G. van der Laan, T. Hesjedal, *J. Magn. Magn. Mater.* **2017**, *422*, 93.
[85] B. A. Aronzon, L. N. Oveshnikov, V. A. Prudkoglyad, Y. G. Selivanov, E. G. Chizhevskii, K. I. Kugel, I. A. Karateev, A. L. Vasiliev, E. Lähderanta, *J. Magn. Magn.Mater.* **2018**, *459*, 331.
[86] L. B. Duffy, N.-J. Steinke, J. A. Krieger, A. I. Figueroa, K. Kummer, T. Lancaster, S. R. Giblin, F. L. Pratt, S. J. Blundell, T. Prokscha, A. Suter, S. Langridge, V. N. Strocov, Z. Salman, G. van der Laan, T. Hesjedal, *Phys. Rev. B* **2018**, *97*, 174427.
[87] L. B. Duffy, A. Frisk, D. M. Burn, N.-J. Steinke, J. Herrero-Martin, A. Ernst, G. van der Laan, T. Hesjedal, *Phys. Rev. Mater.* **2018**, *2*, 054201.
[88] L. B. Duffy, N.-J. Steinke, D. M. Burn, A. Frisk, L. Lari, B. Kuerbanjiang, V. K. Lazarov, G. van der Laan, S. Langridge, T. Hesjedal, *Phys. Rev. B* **2019**, *100*, 054402.
[89] W. Liu, L. He, Y. Xu, K. Murata, M. C. Onbasli, M. Lang, N. J. Maltby, S. Li, X. Wang, C. A. Ross, P. Bencok, G. van der Laan, R. Zhang, K. L. Wang, *Nano Lett.* **2015**, *15*, 764.
[90] C. Tang, C.-Z. Chang, G. Zhao, Y. Liu, Z. Jiang, C.-X. Liu, M. R. McCartney, D. J. Smith, T. Chen, J. S. Moodera, J. Shi, *Sci. Adv.* **2017**, *3*, e1700307.
[91] I. Vobornik, U. Manju, J. Fujii, F. Borgatti, P. Torelli, D. Krizmancic, Y. S. Hor, R. J. Cava, G. Panaccione, *Nano Lett.* **2011**, *11*, 4079.
[92] A. A. Baker, A. I. Figueroa, K. Kummer, L. J. Collins-McIntyre, T. Hesjedal, G. van der Laan, *Phys. Rev. B* **2015**, *92*, 094420.
[93] L. B. Duffy, A. I. Figueroa, L. Gladczuk, N.-J. Steinke, K. Kummer, G. van der Laan, T. Hesjedal, *Phys. Rev. B* **2017**, *95*, 224422.
[94] Q. L. He, X. Kou, A. J. Grutter, G. Yin, L. Pan, X. Che, Y. Liu, T. Nie, B. Zhang, S. M. Disseler, B. J. Kirby, W. Ratcliff II, Q. Shao, K. Murata, X. Zhu, G. Yu, Y. Fan, M. Montazeri, X. Han, J. A. Borchers, K. L. Wang, *Nat. Mater.* **2017**, *16*, 94.
[95] D. S. Lee, T.-H. Kim, C.-H. Park, C.-Y. Chung, Y. S. Lim, W.-S. Seo, H.-H. Park, *Cryst. Eng. Comm.* **2013**, *15*, 5532.
[96] R. C. Vidal, A. Zeugner, J. I. Facio, R. Ray, M. H. Haghighi, A. U. B. Wolter, L. T. Corredor Bohorquez, F. Caglieris, S. Moser, T. Figgemeier, T. R. F. Peixoto, H. B. Vasili, M. Valvidares, S. Jung, C. Cacho, A. Alfonsov, K. Mehlawat, V. Kataev, C. Hess, M. Richter, B. Büchner, J. van den Brink, M. Ruck, F. Reinert, H. Bentmann, A. Isaeva, *Phys. Rev. X* **2019**, *9*, 041065.
[97] E. D. L. Rienks, S. Wimmer, J. Sánchez-Barriga, O. Caha, P. S. Mandal, J. Ružička, A. Ney, H. Steiner, V. V. Volobuev, H. Groiß, M. Albu, G. Kothleitner, J. Michalička, S. A. Khan, J. Minár, H. Ebert, G. Bauer, F. Freyse, V. Varykhalov, O. Rader, G. Springholz, *Nature* **2019**, *576*, 423.
[98] J. A. Hagmann, X. Li, S. Chowdhury, S.-N. Dong, S. Rouvimov, S. J. Pookpanratana, K. M. Yu, T. A. Orlova, T. B. Bolin, C. U. Segre,

D. G. Seiler, C. A. Richter, X. Liu, M. Dobrowolska, J. K. Furdyna, *New J. Phys* **2017**, *19*, 085002.
[99] A. Zeugner, F. Nietschke, A. U. Wolter, S. Gaß, R. C. Vidal, T. R. Peixoto, D. Pohl, C. Damm, A. Lubk, R. Hentrich, S. K. Moser, C. Fornari, C. H. Min, S. Schatz, K. Kißner, M. ünzelmann, M. Kaiser, F. Scaravaggi, B. Rellinghaus, K. Nielsch, C. Hess, B. Büchner, F. Reinert, H. Bentmann, O. Oeckler, T. Doert, M. Ruck, A. Isaeva, *Chem. Mater.* **2019**, *31*, 2795.
[100] S. V. Eremeev, M. M. Otrokov, E. V. Chulkov, *J. Alloys Compd.* **2017**, *709*, 172.
[101] Z. Liu, X. Wei, J. Wang, H. Pan, F. Ji, F. Xi, J. Zhang, T. Hu, S. Zhang, Z. Jiang, W. Wen, Y. Huang, M. Ye, Z. Yang, S. Qiao, *Phys. Rev. B* **2014**, *90*, 094107.
[102] A. I. Figueroa, G. van der Laan, L. J. Collins-McIntyre, G. Cibin, A. J. Dent, T. Hesjedal, *J. Phys. Chem. C* **2015**, *119*, 17344.
[103] A. Karma, M. Plapp, *Phys. Rev. Lett.* **1998**, *81*, 4444.
[104] Y. Liu, M. Weinert, L. Li, *Phys. Rev. Lett.* **2012**, *108*, 115501.
[105] D. D. dos Reis, L. Barreto, M. Bianchi, G. A. S. Ribeiro, E. A. Soares, W. S. Silva, V. E. de Carvalho, J. Rawle, M. Hoesch, C. Nicklin, W. P. Fernandes, J. Mi, B. B. Iversen, P. Hofmann, *Phys. Rev. B* **2013**, *88*, 041404.
[106] H. Yang, A. Liang, C. Chen, C. Zhang, N. B. M. Schroeter, Y. Chen, *Nat. Rev. Mater.* **2018**, *3*, 341.
[107] B. Lv, T. Qian, H. Ding, *Nat. Rev. Phys.* **2019**, *1*, 609.
[108] Y. Zhang, K. He, C.-Z. Chang, C.-L. Song, L.-L. Wang, X. Chen, J.-F. Jia, Z. Fang, X. Dai, W.-Y. Shan, S.-Q. Shen, Q. Niu, X.-L. Qi, S.-C. Zhang, X.-C. Ma, Q.-K. Xue, *Nat. Phys.* **2010**, *6*, 584.
[109] D. Hsieh, D. Qian, L. Wray, Y. Xia, Y. S. Hor, R. J. Cava, M. Z. Hasan, *Nature* **2008**, *452*, 970.
[110] Y. Xia, D. Qian, D. Hsieh, L. Wray, A. Pal, H. Lin, A. Bansil, D. Grauer, Y. S. Hor, R. J. Cava, M. Z. Hasan, *Nat. Phys.* **2009**, *5*, 398.
[111] Y. L. Chen, J. G. Analytis, J.-H. Chu, Z. K. Liu, S.-K. Mo, X.-L. Qi, H. J. Zhang, D. H. Lu, X. Dai, Z. Fang, S. C. Zhang, I. R. Fisher, Z. Hussain, Z.-X. Shen, *Science* **2009**, *325*, 178.
[112] Y. L. Chen, J.-H. Chu, J. G. Analytis, Z. K. Liu, K. Igarashi, H.-H. Kuo, X. L. Qi, S.-K. Mo, R. G. Moore, D. H. Lu, M. Hashimoto, T. Sasagawa, S. C. Zhang, I. R. Fisher, Z. Hussain, Z. X. Shen, *Science* **2010**, *329*, 659.
[113] S. H. Yao, B. Zhou, M. H. Lu, Z. K. Liu, Y. B. Chen, J. G. Analytis, C. Brüne, W. H. Dang, S.-K. Mo, Z.-X. Shen, I. R. Fisher, L. W. Molenkamp, H. L. Peng, Z. Hussain, Y. L. Chen, *Phys. Status Solidi RRL* **2013**, *7*, 130.
[114] L. Plucinski, G. Mussler, J. Krumrain, A. Herdt, S. Suga, D. Grützmacher, C. M. Schneider, *Appl. Phys. Lett.* **2011**, *98*, 222503.
[115] S. E. Harrison, B. Zhou, Y. Huo, A. Pushp, A. J. Kellock, S. S. P. Parkin, J. S. Harris, Y. Chen, T. Hesjedal, *Appl. Phys. Lett.* **2014**, *105*, 121608.
[116] S. Li, S. E. Harrison, Y. Huo, A. Pushp, H. T. Yuan, B. Zhou, A. J. Kellock, S. S. P. Parkin, Y.-L. Chen, T. Hesjedal, J. S. Harris, *Appl. Phys. Lett.* **2013**, *102*, 242412.
[117] G. van der Laan, A. I. Figueroa, *Coord. Chem. Rev.* **2014**, *277-278*, 95.
[118] B. T. Thole, G. van der Laan, J. C. Fuggle, G. A. Sawatzky, R. C. Karnatak, J.-M. Esteva, *Phys. Rev. B* **1985**, *32*, 5107.
[119] A. A. Freeman, K. W. Edmonds, N. R. S. Farley, S. V. Novikov, R. P. Campion, C. T. Foxon, B. L. Gallagher, E. Sarigiannidou, G. van der Laan, *Phys. Rev. B* **2007**, *76*, 081201.
[120] M. D. Watson, L. J. Collins-McIntyre, L. R. Shelford, A. I. Coldea, D. Prabhakaran, S. C. Speller, T. Mousavi, C. R. M. Grovenor, Z. Salman, S. R. Giblin, G. van der Laan, T. Hesjedal, *New J. Phys.* **2013**, *15*, 103016.
[121] B. T. Thole, P. Carra, F. Sette, G. van der Laan, *Phys. Rev. Lett.* **1992**, *68*, 1943.
[122] J. Stöhr, *J. Magn. Magn. Mater.* **1999**, *200*, 470.
[123] G. van der Laan, *J. Phys.: Conf. Ser.* **2013**, *430*, 012127.
[124] A. Arrott, J. E. Noakes, *Phys. Rev. Lett.* **1967**, *19*, 786.
[125] G. van der Laan, *Phys. Rev. Lett.* **1999**, *82*, 640.
[126] A. I. Figueroa, S. E. Harrison, L. J. Collins-McIntyre, G. van der Laan, T. Hesjedal, *Phys. Status Solidi RRL* **2016**, *10*, 467.
[127] A. M. Shikin, D. A. Estyunin, Y. I. Surnin, A. V. Koroleva, E. V. Shevchenko, K. A. Kokh, O. E. Tereshchenko, S. Kumar, E. F. Schwier, K. Shimada, T. Yoshikawa, Y. Saitoh, Y. Takeda, A. Kimura, *Sci. Rep.* **2019**, *9*, 4813.
[128] S. J. Blundell, J. A. C. Bland, *Phys. Rev. B* **1992**, *46*, 3391.
[129] H. Zabel, *Mater. Today* **2006**, *9*, 42.
[130] J. F. Ankner, G. P. Felcher, *J. Magn. Magn. Mater.* **1999**, *200*, 741.
[131] M. Björck, G. Andersson, *J. Appl. Cryst.* **2007**, *40*, 1174.
[132] M. Li, Q. Song, W. Zhao, J. A. Garlow, T.-H. Liu, L. Wu, Y. Zhu, J. S. Moodera, M. H. W. Chan, G. Chen, C.-Z. Chang, *Phys. Rev. B* **2017**, *96*, 201301.
[133] C.-Y. Yang, L. Pan, A. J. Grutter, H. Wang, X. Che, Q. L. He, Y. Wu, D. A. Gilbert, P. Shafer, E. Arenholz, H. Wu, G. Yin, P. Deng, J. A. Borchers, W. Ratcliff, K. L. Wang, *Sci. Adv.* **2020**, *6*, eaaz8463.
[134] A. Hubert, R. Schäfer, *Magnetic Domains—The Analysis of Magnetic Microstructures*, Springer, Berlin, Germany **1998**.
[135] F. Bitter, *Phys. Rev.* **1932**, *41*, 507.
[136] Y. Tokura, K. Yasuda, A. Tsukazaki, *Nat. Rev. Phys.* **2019**, *1*, 126.
[137] J. N. Chapman, *J. Phys. D: Appl. Phys.* **1984**, *17*, 623.
[138] R. Allenspach, *IBM J. Res. Dev.* **2000**, *44*, 553.
[139] L. Yu, W. Wan, T. Koshikawa, M. Li, X. Yang, C. Zheng, M. Suzuki, T. Yasue, X. Jin, Y. Takeda, R. Tromp, W.-X. Tang, *Ultramicroscopy* **2020**, *216*, 113017.
[140] Z. Q. Qiu, S. D. Bader, *J. Magn. Magn. Mater.* **1999**, *200*, 664.
[141] P. N. Argyres, *Phys. Rev.* **1955**, *97*, 334.
[142] L. Pan, X. Liu, Q. L. He, A. Stern, G. Yin, X. Che, Q. Shao, P. Zhang, P. Deng, C.-Y. Yang, B. Casas, E. S. Choi, J. Xia, X. Kou, K. L. Wang, *Sci. Adv.* **2020**, *6*, eaaz3595.
[143] C. Stamm, C. Murer, M. Berritta, J. Feng, M. Gabureac, P. M. Oppeneer, P. Gambardella, *Phys. Rev. Lett.* **2017**, *119*, 087203.
[144] A. Singh, V. S. Kamboj, J. Liu, J. Llandro, L. B. Duffy, S. P. Senanayak, H. E. Beere, A. Ionescu, D. A. Ritchie, T. Hesjedal, C. H. W. Barnes, *Sci. Rep.* **2018**, *8*, 17024.
[145] J. Liu, A. Singh, J. Llandro, L. B. Duffy, M. R. Stanton, S. N. Holmes, M. J. Applegate, R. T. Phillips, T. Hesjedal, C. H. W. Barnes, *Meas. Sci. Technol.* **2019**, *30*, 125201.
[146] Q. I. Yang, M. Dolev, L. Zhang, J. Zhao, A. D. Fried, E. Schemm, M. Liu, A. Palevski, A. F. Marshall, S. H. Risbud, A. Kapitulnik, *Phys. Rev. B* **2013**, *88*, 081407.
[147] A. L. Yeats, P. J. Mintun, Y. Pan, A. Richardella, B. B. Buckley, N. Samarth, D. D. Awschalom, *Proc. Natl. Acad. Sci. USA* **2017**, *114*, 10379.
[148] M. Lang, M. Montazeri, M. C. Onbasli, X. Kou, Y. Fan, P. Upadhyaya, K. Yao, F. Liu, Y. Jiang, W. Jiang, K. L. Wong, G. Yu, J. Tang, T. Nie, L. He, R. N. Schwartz, Y. Wang, C. A. Ross, K. L. Wang, *Nano Lett.* **2014**, *14*, 3459.
[149] J. McCord, *J. Phys. D: Appl. Phys.* **2015**, *48*, 333001.
[150] W. Jiang, P. Upadhyaya, W. Zhang, G. Yu, M. B. Jungfleisch, F. Y. Fradin, J. E. Pearson, Y. Tserkovnyak, K. L. Wang, O. Heinonen, S. G. E. te Velthuis, A. Hoffmann, *Science* **2015**, *349*, 283.
[151] Y. Wang, D. Zhu, Y. Wu, Y. Yang, J. Yu, R. Ramaswamy, R. Mishra, S. Shi, M. Elyasi, K.-L. Teo, Y. Wu, H. Yang, *Nat. Commun.* **2017**, *8*, 1364.
[152] B. D. Huey, J. Luria, D. A. Bonnell, in *Springer Handbook of Microscopy* (Eds: P. W. Hawkes, J. C. H. Spence), Springer, Cham, Switzerland **2019**.
[153] P. Roushan, J. Seo, C. V. Parker, Y. S. Hor, D. Hsieh, D. Qian, A. Richardella, M. Z. Hasan, R. J. Cava, A. Yazdani, *Nature* **2009**, *460*, 1106.

[154] L. Abelmann, S. Porthun, M. Haast, C. Lodder, A. Moser, M. E. Best, P. J. van Schendel, B. Stiefel, H. J. Hug, G. P. Heydon, A. Farley, S. R. Hoon, T. Pfaffelhuber, R. Proksch, K. Babcock, *J. Magn. Magn. Mater.* **1998**, *190*, 135.
[155] J. Mohanty, R. Engel-Herbert, T. Hesjedal, *Appl. Phys. A* **2005**, *81*, 1359.
[156] S. L. Zhang, A. Bauer, D. M. Burn, P. Milde, E. Neuber, L. M. Eng, H. Berger, C. Pfleiderer, G. van der Laan, T. Hesjedal, *Nano Lett.* **2016**, *16*, 3285.
[157] A. M. Chang, H. D. Hallen, L. Harriott, H. F. Hess, H. L. Kao, J. Kwo, R. E. Miller, R. Wolfe, J. van der Ziel, T. Y. Chang, *Appl. Phys. Lett.* **1992**, *61*, 1974.
[158] J. R. Kirtley, J. P. Wikswo, *Annu. Rev. Mater. Res.* **1999**, *29*, 117.
[159] U. Kaiser, A. Schwarz, R. Wiesendanger, *Nature* **2007**, *446*, 522.
[160] Y.-T. Cui, E. Y. Ma, Z.-X. Shen, *Rev. Sci. Instrum.* **2016**, *87*, 063711.
[161] M. Allen, Y. Cui, E. Yue Ma, M. Mogi, M. Kawamura, I. C. Fulga, D. Goldhaber-Gordon, Y. Tokura, Z.-X. Shen, *Proc. Natl. Acad. Sci.* **2019**, *116*, 14511.
[162] M. König, M. Baenninger, A. G. F. Garcia, N. Harjee, B. L. Pruitt, C. Ames, P. Leubner, C. Brüne, H. Buhmann, L. W. Molenkamp, D. Goldhaber-Gordon, *Phys. Rev. X* **2013**, *3*, 021003.
[163] C. M. Schneider, G. Schönhense, *Rep. Prog. Phys.* **2002**, *65*, 1785.
[164] R. Fink, M. R. Weiss, E. Umbach, D. Preikszas, H. Rose, R. Spehr, P. Hartel, W. Engel, R. Degenhardt, R. Wichtendahl, H. Kuhlenbeck, W. Erlebach, K. Ihmann, R. Schlögl, H.-J. Freund, A. M. Bradshaw, G. Lilienkamp, T. Schmidt, E. Bauer, G. Benner, *J. Electron Spectrosc. Relat. Phenom.* **1997**, *84*, 231.
[165] S. Zhang, F. Kronast, G. van der Laan, T. Hesjedal, *Nano Lett.* **2018**, *18*, 1057.
[166] F. Kronast, J. Schlichting, F. Radu, S. K. Mishra, T. Noll, H. A. Dürr, *Surf. Interface Anal.* **2010**, *42*, 1532.
[167] L. Gierster, L. Pape, A. A. Ünal, F. Kronast, *Rev. Sci. Instrum.* **2015**, *86*, 023702.
[168] S. J. Blundell, *Contemp. Phys.* **1999**, *40*, 175.
[169] V. G. Storchak, D. G. Eshchenko, E. Morenzoni, T. Prokscha, A. Suter, X. Liu, J. K. Furdyna, *Phys. Rev. Lett.* **2008**, *101*, 027202.
[170] J. Krieger, Y. Ou, M. Caputo, A. Chikina, M. Döbeli, M.-A. Husanu, I. Keren, T. Prokscha, A. Suter, C.-Z. Chang, J. S. Moodera, V. N. Strocov, Z. Salman, *Phys. Rev. B* **2019**, *99*, 064423.
[171] J. G. Checkelsky, R. Yoshimi, A. Tsukazaki, K. S. Takahashi, Y. Kozuka, J. Falson, M. Kawasaki, Y. Tokura, *Nat. Phys.* **2014**, *10*, 731.
[172] A. Bestwick, E. Fox, X. Kou, L. Pan, K. L. Wang, D. Goldhaber-Gordon, *Phys. Rev. Lett.* **2015**, *114*, 187201.
[173] L. Wu, M. Salehi, N. Koirala, J. Moon, S. Oh, N. P. Armitage, *Science* **2016**, *354*, 1124.
[174] V. S. Kamboj, A. Singh, T. Ferrus, H. E. Beere, L. B. Duffy, T. Hesjedal, C. H. W. Barnes, D. A. Ritchie, *ACS Photonics* **2017**, *4*, 2711.
[175] K. N. Okada, Y. Takahashi, M. Mogi, R. Yoshimi, A. Tsukazaki, K. S. Takahashi, N. Ogawa, M. Kawasaki, Y. Tokura, *Nat. Commun.* **2016**, *7*, 12245.
[176] V. Dziom, A. Shuvaev, A. Pimenov, G. V. Astakhov, C. Ames, K. Bendias, J. Böttcher, G. Tkachov, E. M. Hankiewicz, C. Brüne, H. Buhmann, L. W. Molenkamp, *Nat. Commun.* **2017**, *8*, 15197.
[177] J. S. Dyck, i. c. v. Drašar, P. Lošťák, C. Uher, *Phys. Rev. B* **2005**, *71*, 115214.
[178] X. Kou, S.-T. Guo, Y. Fan, L. Pan, M. Lang, Y. Jiang, Q. Shao, T. Nie, K. Murata, J. Tang, Y. Wang, L. He, T.-K. Lee, W.-L. Lee, K. L. Wang, *Phys. Rev. Lett.* **2014**, *113*, 137201.
[179] L. B. Duffy, A. I. Figueroa, G. van der Laan, T. Hesjedal, *Phys. Rev. Mater.* **2017**, *1*, 064409.
[180] R. Dingle, H. L. Störmer, A. C. Gossard, W. Wiegmann, *Appl. Phys. Lett.* **1978**, *33*, 665.
[181] S. V. Eremeev, V. N. Men, V. V. Tugushev, E. V. Chulkov, *J. Magn. Magn. Mater.* **2015**, *383*, 30.
[182] M. Li, C.-Z. Chang, B. J. Kirby, M. E. Jamer, W. Cui, L. Wu, P. Wei, Y. Zhu, D. Heiman, J. Li, J. S. Moodera, *Phys. Rev. Lett.* **2015**, *115*, 087201.
[183] J. Kim, K.-W. Kim, H. Wang, J. Sinova, R. Wu, *Phys. Rev. Lett.* **2017**, *119*, 027201.
[184] Q. I. Yang, A. Kapitulnik, *Phys. Rev. B* **2018**, *98*, 081403.
[185] P. Wei, F. Katmis, B. A. Assaf, H. Steinberg, P. Jarillo-Herrero, D. Heiman, J. S. Moodera, *Phys. Rev. Lett.* **2013**, *110*, 186807.
[186] F. Katmis, V. Lauter, F. S. Nogueira, B. A. Assaf, M. E. Jamer, P. Wei, B. Satpati, J. W. Freeland, I. Eremin, D. Heiman, P. Jarillo-Herrero, J. S. Moodera, *Nature* **2016**, *533*, 513.
[187] C. Lee, F. Katmis, P. Jarillo-Herrero, J. S. Moodera, N. Gedik, *Nat. Commun.* **2016**, *7*, 12014.
[188] A. I. Figueroa, F. Bonell, M. G. Cuxart, M. Valvidares, P. Gargiani, G. van der Laan, A. Mugarza, S. O. Valenzuela, *Phys. Rev. Lett.* **2020**, *125*, 226801.
[189] Y. J. Chen, L. X. Xu, J. H. Li, Y. W. Li, H. Y. Wang, C. F. Zhang, H. Li, Y. Wu, A. J. Liang, C. Chen, S. W. Jung, C. Cacho, Y. H. Mao, S. Liu, M. X. Wang, Y. F. Guo, Y. Xu, Z. K. Liu, L. X. Yang, Y. L. Chen, *Phys. Rev. X* **2019**, *9*, 041040.
[190] V. M. Pereira, S. G. Altendorf, C. E. Liu, S. C. Liao, A. C. Komarek, M. Guo, H.-J. Lin, C. T. Chen, M. Hong, J. Kwo, L. H. Tjeng, C. N. Wu, *Phys. Rev. Mater.* **2020**, *4*, 064202.
[191] Z. Jiang, F. Katmis, C. Tang, P. Wei, J. S. Moodera, J. Shi, *Appl. Phys. Lett.* **2014**, *104*, 222409.
[192] W. Liu, L. He, Y. Xu, K. Murata, M. C. Onbasli, M. Lang, N. J. Maltby, S. Li, X. Wang, C. A. Ross, P. Bencok, G. van der Laan, R. Zhang, K. L. Wang, *Nano Lett.* **2015**, *15*, 764.
[193] Z. Jiang, C.-Z. Chang, C. Tang, P. Wei, J. S. Moodera, J. Shi, *Nano Lett.* **2015**, *15*, 5835.
[194] Z. Jiang, C.-Z. Chang, M. R. Masir, C. Tang, Y. Xu, J. S. Moodera, A. H. MacDonald, J. Shi, *Nat. Commun.* **2016**, *7*, 11458.
[195] X. Che, K. Murata, L. Pan, Q. L. He, G. Yu, Q. Shao, G. Yin, P. Deng, Y. Fan, B. Ma, X. Liang, B. Zhang, X. Han, L. Bi, Q.-H. Yang, H. Zhang, K. L. Wang, *ACS Nano* **2018**, *12*, 5042.
[196] Y. T. Fanchiang, K. H. M. Chen, C. C. Tseng, C. C. Chen, C. K. Cheng, S. R. Yang, C. N. Wu, S. F. Lee, M. Hong, J. Kwo, *Nat. Commun.* **2018**, *9*, 223.
[197] T. Liu, J. Kally, T. Pillsbury, C. Liu, H. Chang, J. Ding, Y. Cheng, M. Hilse, R. Engel-Herbert, A. Richardella, N. Samarth, M. Wu, *Phys. Rev. Lett.* **2020**, *125*, 017204.
[198] L. D. Alegria, H. Ji, N. Yao, J. J. Clarke, R. J. Cava, J. R. Petta, *Appl. Phys. Lett.* **2014**, *105*, 053512.
[199] M. Mogi, T. Nakajima, V. Ukleev, A. Tsukazaki, R. Yoshimi, M. Kawamura, K. S. Takahashi, T. Hanashima, K. Kakurai, T.-h. Arima, M. Kawasaki, Y. Tokura, *Phys. Rev. Lett.* **2019**, *123*, 016804.
[200] M. Mogi, K. Yasuda, R. Fujimura, R. Yoshimi, N. Ogawa, A. Tsukazaki, M. Kawamura, K. S. Takahashi, M. Kawasaki, Y. Tokura, *Nat. Commun.* **2021**, *12*, 1404.
[201] W. Yang, S. Yang, Q. Zhang, Y. Xu, S. Shen, J. Liao, J. Teng, C. Nan, L. Gu, Y. Sun, K. Wu, Y. Li, *Appl. Phys. Lett.* **2014**, *105*, 092411.
[202] P. Li, J. Kally, S. S. L. Zhang, T. Pillsbury, J. Ding, G. Csaba, J. Ding, J. S. Jiang, Y. Liu, R. Sinclair, C. Bi, A. DeMann, G. Rimal, W. Zhang, S. B. Field, J. Tang, W. Wang, O. G. Heinonen, V. Novosad, A. Hoffmann, N. Samarth, M. Wu, *Sci. Adv.* **2019**, *5*, eaaw3415.
[203] T. Hesjedal, *Phys. Status Solidi A* **2019**, *216*, 1800726.
[204] J. Kim, K. Lee, T. Takabatake, H. Kim, M. Kim, M.-H. Jung, *Sci. Rep.* **2015**, *5*, 10309.
[205] S.-W. Kim, M.-H. Jung, *Appl. Phys. Lett.* **2018**, *112*, 202401.

[206] T. Chen, W. Liu, F. Zheng, M. Gao, X. Pan, G. van der Laan, X. Wang, Q. Zhang, F. Song, B. Wang, B. Wang, Y. Xu, G. Wang, R. Zhang, *Adv. Mater.* **2015**, *27*, 4823.
[207] C. Yue, Y. Xu, Z. Song, H. Weng, Y.-M. Lu, C. Fang, X. Dai, *Nat. Phys.* **2019**, *15*, 577.
[208] A. I. Figueroa, G. van der Laan, S. E. Harrison, G. Cibin, T. Hesjedal, *Sci. Rep.* **2016**, *6*, 22935.
[209] D. R. Behrendt, S. Legvold, F. H. Spedding, *Phys. Rev.* **1958**, *109*, 1544.
[210] J. Liu, A. Singh, Y. Y. F. Liu, A. Ionescu, B. Kuerbanjiang, C. H. W. Barnes, T. Hesjedal, *Nano Lett.* **2020**, *20*, 5315.
[211] P. K. Manna, S. M. Yusuf, *Phys. Rep.* **2014**, *535*, 61.
[212] J. Sort, F. Garcia, S. Auffret, B. Rodmacq, B. Dieny, V. Langlais, S. Suriñach, J. S. Muñoz, M. D. Baró, J. Nogués, *Appl. Phys. Lett.* **2005**, *87*, 242504.
[213] C. Won, Y. Z. Wu, H. W. Zhao, A. Scholl, A. Doran, W. Kim, T. L. Owens, X. F. Jin, Z. Qiu, *Phys. Rev. B* **2005**, *71*, 024406.
[214] K. Lenz, S. Zander, W. Kuch, *Phys. Rev. Lett.* **2007**, *98*, 237201.
[215] Q. L. He, X. Kou, A. J. Grutter, G. Yin, L. Pan, X. Che, Y. Liu, T. Nie, B. Zhang, S. M. Disseler, B. J. Kirby, W. Ratcliff II, Q. Shao, K. Murata, X. Zhu, G. Yu, Y. Fan, M. Montazeri, X. Han, J. A. Borchers, K. L. Wang, *Nat. Mater.* **2017**, *16*, 94.
[216] F. Wang, D. Xiao, W. Yuan, J. Jiang, Y.-F. Zhao, L. Zhang, Y. Yao, W. Liu, Z. Zhang, C. Liu, J. Shi, W. Han, M. H. W. Chan, N. Samarth, C.-Z. Chang, *Nano Lett.* **2019**, *19*, 2945.
[217] Q. L. He, G. Yin, A. J. Grutter, L. Pan, X. Che, G. Yu, D. A. Gilbert, S. M. Disseler, Y. Liu, P. Shafer, B. Zhang, Y. Wu, B. J. Kirby, E. Arenholz, R. K. Lake, X. Han, K. L. Wang, *Nat. Commun.* **2018**, *9*, 2767.
[218] A. Neubauer, C. Pfleiderer, B. Binz, A. Rosch, R. Ritz, P. G. Niklowitz, P. Böni, *Phys. Rev. Lett.* **2009**, *102*, 186602.
[219] A. Fert, N. Reyren, V. Cros, *Nat. Rev. Mater.* **2017**, *2*, 17031.
[220] X. S. Wang, H. Y. Yuan, X. R. Wang, *Commun. Phys.* **2018**, *1*, 31.
[221] S. S. P. Parkin, M. Hayashi, L. Thomas, *Science* **2008**, *320*, 190.
[222] X. Zhang, M. Ezawa, Y. Zhou, *Sci. Rep.* **2015**, *5*, 9400.
[223] M. Carpentieri, R. Tomasello, R. Zivieri, G. Finocchio, *Sci. Rep.* **2015**, *5*, 16184.
[224] F. Ma, Y. Zhou, H. B. Braun, W. S. Lew, *Nano Lett.* **2015**, *15*, 4029.
[225] N. Nagaosa, Y. Tokura, *Nat. Nanotechnol.* **2013**, *8*, 899.
[226] C. Liu, Y. Zang, W. Ruan, Y. Gong, K. He, X. Ma, Q.-K. Xue, Y. Wang, *Phys. Rev. Lett.* **2017**, *119*, 176809.
[227] K. Yasuda, R. Wakatsuki, T. Morimoto, R. Yoshimi, A. Tsukazaki, K. S. Takahashi, M. Ezawa, M. Kawasaki, N. Nagaosa, Y. Tokura, *Nat. Phys.* **2016**, *12*, 555.
[228] J. Chen, L. Wang, M. Zhang, L. Zhou, R. Zhang, L. Jin, X. Wang, H. Qin, Y. Qiu, J. Mei, F. Ye, B. Xi, H. He, B. Li, G. Wang, *Nano Lett.* **2019**, *19*, 6144.
[229] P. Li, J. Ding, S. S.-L. Zhang, J. Kally, T. Pillsbury, O. G. Heinonen, G. Rimal, C. Bi, A. DeMann, S. B. Field, W. Wang, J. Tang, J. S. Jiang, A. Hoffmann, N. Samarth, M. Wu, *Nano Lett.* **2020**, *21*, 84.
[230] H. Wu, F. Groß, B. Dai, D. Lujan, S. A. Razavi, P. Zhang, Y. Liu, K. Sobotkiewich, J. Förster, M. Weigand, G. Schütz, X. Li, J. Gräfe, K. L. Wang, *Adv. Mater.* **2020**, *32*, 2003380.
[231] W. Wang, Y.-F. Zhao, F. Wang, M. W. Daniels, C.-Z. Chang, J. Zang, D. Xiao, W. Wu, *Nano Lett.* **2021**, *21*, 1108.
[232] J. Jiang, D. Xiao, F. Wang, J.-H. Shin, D. Andreoli, J. Zhang, R. Xiao, Y.-F. Zhao, M. Kayyalha, L. Zhang, K. Wang, J. Zang, C. Liu, N. Samarth, M. H. W. Chan, C.-Z. Chang, *Nat. Mater.* **2020**, *19*, 732.
[233] A. Gerber, *Phys. Rev. B* **2018**, *98*, 214440.
[234] D. Kan, T. Moriyama, K. Kobayashi, Y. Shimakawa, *Phys. Rev. B* **2018**, *98*, 180408.
[235] N. Liu, J. Teng, Y. Li, *Nat. Commun.* **2018**, *9*, 1282.
[236] W. Zhang, B. Balasubramanian, A. Ullah, R. Pahari, X. Li, L. Yue, S. R. Valloppilly, A. Sokolov, R. Skomski, D. J. Sellmyer, *Appl. Phys. Lett.* **2019**, *115*, 172404.
[237] S. Zhang, S. Xia, Q. Cao, D. Wang, R. Liu, Y. Du, *Appl. Phys. Lett.* **2019**, *115*, 022404.
[238] K. M. Fijalkowski, M. Hartl, M. Winnerlein, P. Mandal, S. Schreyeck, K. Brunner, C. Gould, L. W. Molenkamp, *Phys. Rev. X* **2020**, *10*, 011012.
[239] P. Chen, Y. Zhang, Q. Yao, F. Tian, L. Li, Z. Qi, X. Liu, L. Liao, C. Song, J. Wang, J. Xia, G. Li, D. M. Burn, G. van der Laan, T. Hesjedal, S. Zhang, X. Kou, *Nano Lett.* **2020**, *20*, 1731.
[240] J. Liu, A. Singh, B. Kuerbanjiang, C. H. W. Barnes, T. Hesjedal, *Nanotechnology* **2020**, *31*, 434001.
[241] F. Wang, X. Wang, Y.-F. Zhao, D. Xiao, L.-J. Zhou, W. Liu, Z. Zhang, W. Zhao, M. H. W. Chan, N. Samarth, C. Liu, H. Zhang, C.-Z. Chang, *Nat. Commun.* **2021**, *12*, 79.
[242] J. Matsuno, N. Ogawa, K. Yasuda, F. Kagawa, W. Koshibae, N. Nagaosa, Y. Tokura, M. Kawasaki, *Sci. Adv.* **2016**, *2*, e1600304.
[243] S. L. Zhang, A. Bauer, H. Berger, C. Pfleiderer, G. van der Laan, T. Hesjedal, *Phys. Rev. B* **2016**, *93*, 214420.
[244] S. Zhang, G. van der Laan, J. Müller, L. Heinen, M. Garst, A. Bauer, H. Berger, C. Pfleiderer, T. Hesjedal, *Proc. Natl. Acad. Sci. USA* **2018**, *115*, 6386.
[245] K.-Y. Meng, A. S. Ahmed, M. Baćani, A.-O. Mandru, X. Zhao, N. Bagués, B. D. Esser, J. Flores, D. W. McComb, H. J. Hug, F. Yang, *Nano Lett.* **2019**, *19*, 3169.
[246] J. Li, Y. Li, S. Du, Z. Wang, B.-L. Gu, S.-C. Zhang, K. He, W. Duan, Y. Xu, *Sci. Adv.* **2019**, *5*, eaaw5685.
[247] M. M. Otrokov, I. P. Rusinov, M. Blanco-Rey, M. Hoffmann, A. Y. Vyazovskaya, S. V. Eremeev, A. Ernst, P. M. Echenique, A. Arnau, E. V. Chulkov, *Phys. Rev. Lett.* **2019**, *122*, 107202.
[248] D. Zhang, M. Shi, T. Zhu, D. Xing, H. Zhang, J. Wang, *Phys. Rev. Lett.* **2019**, *122*, 206401.
[249] Y. Gong, J. Guo, J. Li, K. Zhu, M. Liao, X. Liu, Q. Zhang, L. Gu, L. Tang, X. Feng, D. Zhang, W. Li, C. Song, L. Wang, P. Yu, X. Chen, Y. Wang, H. Yao, W. Duan, Y. Xu, S.-C. Zhang, X. Ma, Q.-K. Xue, K. He, *Chin. Phys. Lett.* **2019**, *36*, 076801.
[250] S. H. Lee, Y. Zhu, Y. Wang, L. Miao, T. Pillsbury, H. Yi, S. Kempinger, J. Hu, C. A. Heikes, P. Quarterman, W. Ratcliff, J. A. Borchers, H. Zhang, X. Ke, D. Graf, N. Alem, C.-Z. Chang, N. Samarth, Z. Mao, *Phys. Rev. Res.* **2019**, *1*, 012011.
[251] J.-Q. Yan, Q. Zhang, T. Heitmann, Z. Huang, K. Y. Chen, J.-G. Cheng, W. Wu, D. Vaknin, B. C. Sales, R. J. McQueeney, *Phys. Rev. Mater.* **2019**, *3*, 064202.
[252] B. Chen, F. Fei, D. Zhang, B. Zhang, W. Liu, S. Zhang, P. Wang, B. Wei, Y. Zhang, Z. Zuo, J. Guo, Q. Liu, Z. Wang, X. Wu, J. Zong, X. Xie, W. Chen, Z. Sun, S. Wang, Y. Zhang, M. Zhang, X. Wang, F. Song, H. Zhang, D. Shen, B. Wang, *Nat. Commun.* **2019**, *10*, 4469.
[253] C. Liu, Y. Wang, H. Li, Y. Wu, Y. Li, J. Li, K. He, Y. Xu, J. Zhang, Y. Wang, *Nat. Mater.* **2020**, *19*, 522.
[254] D. Ovchinnikov, X. Huang, Z. Lin, Z. Fei, J. Cai, T. Song, M. He, Q. Jiang, C. Wang, H. Li, Y. Wang, Y. Wu, D. Xiao, J.-H. Chu, J. Yan, C.-Z. Chang, Y.-T. Cui, X. Xu, *Nano Lett.* **2021**, *21*, 2544.
[255] Y.-J. Hao, P. Liu, Y. Feng, X.-M. Ma, E. F. Schwier, M. Arita, S. Kumar, C. Hu, M. Zeng, Y. Wang, Z. Hao, H.-Y. Sun, K. Zhang, J. Mei, N. Ni, L. Wu, K. Shimada, C. Chen, Q. Liu, C. Liu, *Phys. Rev. X* **2019**, *9*, 041038.
[256] H. Li, S.-Y. Gao, S.-F. Duan, Y.-F. Xu, K.-J. Zhu, S.-J. Tian, J.-C. Gao, W.-H. Fan, Z.-C. Rao, J.-R. Huang, J.-J. Li, D.-Y. Yan, Z.-T. Liu, W.-L. Liu, Y.-B. Huang, Y.-L. Li, Y. Liu, G.-B. Zhang, P. Zhang, T. Kondo, S. Shin, H.-C. Lei, Y.-G. Shi, W.-T. Zhang, H.-M. Weng, T. Qian, H. Ding, *Phys. Rev. X* **2019**, *9*, 041039.
[257] M. Z. Shi, B. Lei, C. S. Zhu, D. H. Ma, J. H. Cui, Z. L. Sun, J. J. Ying, X. H. Chen, *Phys. Rev. B* **2019**, *100*, 155144.

[258] L. Xu, Y. Mao, H. Wang, J. Li, Y. Chen, Y. Xia, Y. Li, D. Pei, J. Zhang, H. Zheng, K. Huang, C. Zhang, S. Cui, A. Liang, W. Xia, H. Su, S. Jung, C. Cacho, M. Wang, G. Li, Y. Xu, Y. Guo, L. Yang, Z. Liu, Y. Chen, M. Jiang, *Sci. Bull.* **2020**, *65*, 2086.
[259] H. Fu, C.-X. Liu, B. Yan, *Sci. Adv.* **2020**, *6*, eaaz0948.
[260] B. Huang, G. Clark, E. Navarro-Moratalla, D. R. Klein, R. Cheng, K. L. Seyler, D. Zhong, E. Schmidgall, M. A. McGuire, D. H. Cobden, W. Yao, D. Xiao, P. Jarillo-Herrero, X. Xu, *Nature* **2017**, *546*, 270.
[261] B. Huang, M. A. McGuire, A. F. May, D. Xiao, P. Jarillo-Herrero, X. Xu, *Nat. Mater.* **2020**, *19*, 1276.
[262] T. Zhang, Y. Jiang, Z. Song, H. Huang, Y. He, Z. Fang, H. Weng, C. Fang, *Nature* **2019**, *566*, 475.
[263] M. Vergniory, L. Elcoro, C. Felser, N. Regnault, B. A. Bernevig, Z. Wang, *Nature* **2019**, *566*, 480.
[264] Y. Xu, L. Elcoro, Z.-D. Song, B. J. Wieder, M. Vergniory, N. Regnault, Y. Chen, C. Felser, B. A. Bernevig, *Nature* **2020**, *586*, 702.
[265] S.-W. Wang, D. Xiao, Z. Dou, M. Cao, Y.-F. Zhao, N. Samarth, C.-Z. Chang, M. R. Connolly, C. G. Smith, *Phys. Rev. Lett.* **2020**, *125*, 126801.
[266] F. Giustino, J. H. Lee, F. Trier, M. Bibes, S. M. Winter, R. Valentí, Y.-W. Son, L. Taillefer, C. Heil, A. I. Figueroa, B. Plaçais, Q. Wu, O. V. Yazyev, E. P. A. M. Bakkers, J. Nygård, P. Forn-Díaz, S. D. Franceschi, J. W. McIver, L. E. F. F. Torres, T. Low, A. Kumar, R. Galceran, S. O. Valenzuela, M. V. Costache, A. Manchon, E.-A. Kim, G. R. Schleder, A. Fazzio, S. Roche, *J. Phys. Mater.* **2021**, *3*, 042006.
[267] D. M. Burn, L. B. Duffy, R. Fujita, S. L. Zhang, A. I. Figueroa, J. Herrero-Martin, G. van der Laan, T. Hesjedal, *Sci. Rep.* **2019**, *9*, 10793.

Jieyi Liu is a postdoctoral research assistant at the Clarendon Laboratory, University of Oxford. His research is focused on novel electronic structures and magnetic properties of magnetic topological materials using angle-resolved photoemission spectroscopy and X-ray magnetic circular dichroism. Before coming to Oxford, he obtained his Ph.D. degree at the University of Cambridge, where he studied magnetic topological insulators and semiconductor-based spin transport devices through Kerr effect magnetometry.

Thorsten Hesjedal is Professor of Experimental Physics at the University of Oxford. His research is focused on topological thin-film quantum materials, and their magnetic and structural characterization using X-ray and neutron scattering. Before coming to Oxford, he was Associate Professor at the University of Waterloo (Ontario, Canada), Visiting Associate Professor at Stanford University, Visiting Professor at the UC Santa Barbara, and Lecturer at Stanford University (Berlin Overseas Campus).